Applied Physics A (2024) 130:469
https://doi.org/10.1007/s00339-024-07596-3

**Applied Physics A**
**Materials Science & Processing**

# Temperature dependence of Raman scattering in pentasodium trioxoundecafluoro-trititanate

**C. M. Mbulanga[1,2,5] · R. Erasmus[3] · C. C. Ahia[4] · H. Nyengeri[5] · K. S. Niyomugavyi[5] · D. Harerimana[5] · E. L. Meyer[4] · J. R. Botha[2]**

Received: 14 November 2023 / Accepted: 14 May 2024


**Abstract**
Experimental results from temperature dependent Raman spectroscopy measurements which were obtained at room temperature up to 325 °C from pentasodium trioxoundecafluoro-trititanate [$Na_5(Ti_3O_3F_{11})$] powder are reported in the present study. The following Raman lines $A_{1g}$, $B_{1g}$, $B_{2g}$ and $B_{3g}$ show significant broadening and shifting. Two models are used to approximate the temperature-dependent Raman shift and the Full Width at Half Maximum (FWHM) of the observed Raman modes: linear and Klemens models. The Klemens model provides a much better approximation than the linear approximation. Consequently, anharmonic phonon-phonon interactions are considered to be responsible for the observed temperature dependence of the Raman spectra of pentasodium trioxoundecafluoro-trititanate. In addition, it is understood that three- and four-phonon processes combined together contribute to the damping process. Observed redshifts and blueshifts are explicitly attributed to the change in vibrational frequencies due to thermal expansion or to the change in volume resulting from phonon softening induced by the increase in annealing temperature. In more details, the observed blue shifts are attributed to a change in mean vibrational energy at constant volume. Furthermore, it is found that $Na_5(Ti_3O_3F_{11})$ undergoes another phase transition at ~ 300 °C.

**Keywords** Raman blueshift · Raman redshift · Pentasodium trioxoundecafluoro-trititanate · Temperature dependence Raman spectroscopy · Phase transition · Chemical stability

## 1 Introduction

The availability of good quality fresh water is crucial to human development and health. Rising population and average living standards, which have led to water scarcity, combined with environmental concerns, should make it possible to consider water as a resource within the framework of a circular economy. Drinking water treatment is seen as a necessity that has greatly benefited the health of the human population in recent decades. Nowadays, wastewater treatment is also becoming an obligation to meet high standards of reuse, especially in areas where water is scarce, or before discharge into natural ecosystems [1]. This is why environmental pollution by heavy metals has become a major issue worldwide [1–3]. Industries such as electroplating, batteries, printed circuit boards and the treatment of metal surface coatings have proved to be the main sources of pollution of wastewater by heavy metal ions such as Cd, Cu, Ni, Pb and Zn, to name but a few [4]. Lead, for example, can cause a range of neurological diseases and, in some cases, can even be fatal [4]. For these reasons, surface water and wastewater contaminated by these metals must be treated before reuse. To achieve this, user-friendly, inexpensive, and easy-to-use heavy metal sensors/detectors need to be developed.

✉ C. M. Mbulanga
crispin.mbulanga@gmail.com

1 Department of Physics and Applied Physics, Université Pédagogique de Kananga, P.O Box 282, Kananga, Democratic Republic of Congo

2 Department of Physics, Nelson Mandela University, P.O Box 77000, Port Elizabeth 6031, South Africa

3 School of Physics and Microscopy and Microanalysis Unit, University of the Witwatersrand, WITS, Private Bag 3, Johannesburg 2050, South Africa

4 Institute of Technology, University of Fort Hare, Private Bag X1314, Alice 5700, South Africa

5 Department of Physics, Université du Burundi, P.O Box 1550, Bujumbura, Burundi

Published online: 04 June 2024

Several methods have been developed and used for the removal of heavy metals from wastewater, such as chemical precipitation [5], floatation [6], reverse osmosis [7], membrane filtration [8], electrochemical treatment [9] and bioremediation [10]. For the removal of traces of heavy metals from water, adsorption has been considered one of the most attractive and promising methods for removing traces of $Cu^{2+}$, $Pb^{2+}$, $Zn^{2+}$ and $Cd^{2+}$ from water [1, 11–15]. Here's why this method is favored: the adsorption mechanism makes it possible, under mild conditions, to avoid the production of secondary sludge; and in many cases, the adsorbent can be regenerated and reused for several water cycles [11–15]. Materials with these properties can therefore be used to detect heavy metals in water. The most widely studied and used materials for heavy metal removal are alkaline earth metal titanates. However, among the alkaline-earth titanates, "sodium titanates" have taken the lead. These have attracted increasing attention due to their robustness, their particular intercalary chemistry and their great ability to activate ion exchange reactions [15]. Various structures (flowers [16], fibers [17], whiskers [18] and tubes [19]) have been shown to increase the surface area and adsorption capacities of sodium titanates. For example, Huang et al. [20] studied the effect of sodium titanate structure on the adsorption of heavy metals. Titanate nanoflowers showed the best adsorption properties compared to nanotube and nanowire structures, with a maximum Langmuir adsorption capacity of 304 mg/g for $Pb^{2+}$. On the other hand, Hang et al. [18] reported for titanate whiskers an adsorption of 385 mg/g for $Pb^{2+}$. Therefore, we understand that sodium titanates can potentially be used as heavy metal sensors for the following reasons: (i) they interact chemically with heavy metals; (ii) the layered morphology can accommodate the charges and allow them to diffuse a short distance to reach the intercalated position; (iii) the sodium ions existing in the space intercalated between the titanate layers carry negative charges and can be exchanged with other cations; and (iv) they are able to tolerate the deformation of the structure caused by the ion intercalation process due to the layered structure, thus improving cycle stability [20]. Properties (i–iv) can be exploited and used for the fabrication of heavy metal sensors in water.

In 2021, we described and discussed a new route for the synthesis of an epitaxial compound with plate-like morphology on fluorine-doped tin oxide (FTO)-coated glass substrates, identified as pentasodium trioxoundecafluoro-trititanate $Na_5(Ti_3O_3F_{11})$ [21]. The developed $Na_5(Ti_3O_3F_{11})$ samples were found to be "textured with a small number of micrometer-sized crystals among the predominant plate-like structures. These structures were attached to the F:$SnO_2$ (FTO) layer due to their nucleation and growth on the substrate surface during the hydrothermal process" [21], a quality necessary for semiconductor applications requiring electrical contact. This particular structural type is adopted by a number of fluorides, oxides and oxyfluorides with the general formula $A_5M_3X_{14}$ ($X = O_iF_{14-i}$, $i = 0 \ldots 14$). Before pentasodium trioxoundecafluoro-trititanate can be used for the above-mentioned application, a great deal of research is required. This article therefore presents the in-situ temperature-dependent Raman characterization of pentasodium trioxoundecafluoro-trititanate, following the work carried out in reference [21] with the aim of establishing studies on the chemical stability, degradation and phase transition mechanism of $Na_5(Ti_3O_3F_{11})$ plates in argon. These studies are also essential for understanding the structural properties and phononic behaviors of $Na_5(Ti_3O_3F_{11})$. Temperature-dependent Raman studies have already been reported for various semiconductor materials such as $Cu_2ZnSnSe_4$ thin films [22, 23] in order to understand the transition from kesterite to disordered kesterite structures, as this transition can modify the effective bandgap of $Cu_2ZnSnSe_4$. Taube et al. [24] have also studied the temperature-induced phonon behavior of germanium selenide thin films using Raman spectroscopy. Unfortunately, this area of research remains largely unexplored for $Na_5(Ti_3O_3F_{11})$.

## 2 Experimental details

Ammonium hexafluorotitanate (99.99%, metal base), boric acid (98%), NaCl and F:$SnO_2$-coated glass substrates (FTO) were used as supplied. Two types of samples were developed: $Na_5(Ti_3O_3F_{11})$ structures on FTO and in powder form. *Degreasing procedure*: the substrates were cleaned sequentially with hot trichloroethylene (TCE), acetone and methanol, followed by deionized water (DI) rinsing and nitrogen drying. *Precursor preparation*: in a typical plate synthesis, a 90 ml precursor solution consisting of 0.94 M, 24 mM and 56 mM molar concentrations of NaCl (salt), ammonium hexafluorotitanate (salt) and boric acid (salt), respectively, was prepared with deionized water as solvent under vigorous magnetic stirring to form a homogeneous mixture. The mixture was then poured into a Teflon container, which was placed in a stainless-steel autoclave at room temperature. *Sample development:* (i) for plate formation, a cleaned substrate (FTO) was placed in the precursor solution at an angle of ~ 45° against the autoclave wall, with the conductive side facing down. The sealed autoclave was placed in an oven preheated to 100 °C for 2 h [21]. (ii) For powder development, after the $Na_5(Ti_3O_3F_{11})$ development experiment on FTO (experiment (i)), a white precipitate remained, collected by gravity at the bottom of the Teflon container. This precipitate was filtered and washed with distilled water. The washed powder was then dried in a preheated oven at

**Table 1** List of samples developed by hydrothermal method

| Sample number | Name of samples | Chemical identity | Substrate orientation in the autoclave |
|---|---|---|---|
| 1 | HB-Exp 1-2h-290323-1 | $Na_5(Ti_3O_3F_{11})$ on FTO | Facing down |
| 2 | HB-Exp 1-2h-100423-1 | $Na_5(Ti_3O_3F_{11})$ on FTO | Facing down |
| 3 | HD-EXP 1-2h-100423-1-Powder | $Na_5(Ti_3O_3F_{11})$ powder | – |

100 °C. Table 1 contain details of the samples developed: HB-Exp 1-2h-290323-1 and HB-Exp 1-2h-100423-1. They were developed according to the procedure described above for the development of $Na_5(Ti_3O_3F_{11})$ on FTO. Numbers "290323" correspond to March 29, 2023 and "100423: to April 10, 2023. They therefore differ only in that they result from two different experiments carried out on different days. Sample HD-EXP 1-2h-100423-1-Powder is the powder collected from the precursor solution at the end of the experiment to develop sample HD-EXP 1-2h-100423-1.

A WITec alpha300 series confocal Raman microscope system with modular design was used to acquire room temperature Raman spectra. The WITec system is equipped with a UHTS300S VIS spectrometer and a highly linear (0.02%) piezo-driven scan stage. Furthermore, the high throughput spectrometer is furnished with a 600 g/mm grating and a blaze wavelength of 500 nm. Prior to data acquisition, the system was routinely calibrated by investigating/using the second order Si line as reference. The images from the samples were properly focused using a 20 × Zeiss Epiplan objective with numerical aperture of 0.4. An excitation wavelength of 532 nm and a laser power of 39 mW was used for all scans. A spectral integration time of 1.0 s for 30 numbers of accumulations was adopted in all cases during Raman spectral acquisition. For temperature dependent in-situ Raman characterisation, the 514.5 nm line of an argon ion laser was used with a Horiba LabRAM HR Raman spectrometer, equipped with an Olympus BX41 micro-Raman attachment. The Raman spectra were recorded in the backscattering configuration. Sample temperature was varied using a Linkam TS1500 microscope oven under argon atmosphere. The backscattered signal was dispersed via a 600 line/mm grating on a liquid nitrogen-cooled CCD detector, and the signal was acquired using LabSpec v5 software. The excitation Raman laser spot was 2 µm in diameter.

## 3 Results and discussion

Figure 1 shows (a–c) room temperature Raman spectra of all samples listed in Table 1 (d) 2D mapping Raman spectra of sample number 3 (HD-EXP 1-2h-290323-1-Powder); and (e) figure (d) plotted over 100–300 $cm^{-1}$ for clarity. It should be noted that the determination of Raman shift positions presented here agree with the results reported in reference [21]. Indeed, Fig. 1a–c shows a very good match between these two spectra in terms of Raman shift positions, with the exception of the Raman shift observed at ~ 144 $cm^{-1}$. A summary of these Raman shifts is given in Table 2. From Fig. 1d, e, it is seen that the peak at ~ 144 $cm^{-1}$ is not present in all Raman spectra. Furthermore, the Raman spectra collected over a large area of powder (see Fig. 1d, e) confirm the presence of the peak detected at ~ 144 $cm^{-1}$ in Fig. 1b. There is no doubt that traces of the material responsible for the Raman shift at ~ 144 $cm^{-1}$ are present on both as-grown structures developed on FTO and in the powder form. It can primarily be concluded that the structure developed on FTO and the one collected in powder form consist of the same compound, as expected namely pentasodium trioxoundecafluoro-trititanate [21]. Furthermore, according to information from the Bilbao crystallographic server for the Cmce space group (No. 64) to which the crystal structure of pentasodium trioxoundecafluoro-trititanate belongs, the optical vibration modes involved are [21, 25]:

$$\begin{aligned}\Gamma_{vib} =& 6A_g(\text{Raman}) + 6B_{1g}(\text{Raman}) \\ &+ 5B_{2g}(\text{Raman}) + 7B_{3g}(\text{Raman}) \\ &+ 13B_{1u}(\text{IR}) + 12B_{2u}(\text{IR}) + 10B(\text{IR})\end{aligned} \quad (1)$$

From Eq. (1), we understand that there are a total of 24 active Raman vibrations grouped into the following vibration modes: $A_g$, $B_{1g}$, $B_{2g}$ and $B_{3g}$. These modes of vibration originate from atomic vibrations involving 13 crystallographic sites, namely Na1 (site 4a), Na2 (site 8f), Na3 (site 8e), Ti1 (site 4b), Ti2 (site 8c), O1 (site 16 g), O2 (site 16 g), O3 (site 16 g), O4 (site 8f), F1 (site 16 g), F2 (site 16 g), F3 (site 16 g) and F4 (site 8f) [25]. In addition, it has been suggested (based on experimental observations [21]) that of all the 13 crystallographic sites, only atoms located at the following sites participate in active Raman vibrations: site 4a (atom Na1), site 8f (atom Na2), site 8e (atom Na3), site 16 g (atom O1), site 8f (atom O4) and site 16f (atoms F1, F2 and F3). By way of illustration, the crystallographic sites of the atoms whose vibrations are responsible for the observed Raman shifts are shown in Fig. 2 and Fig. 3.

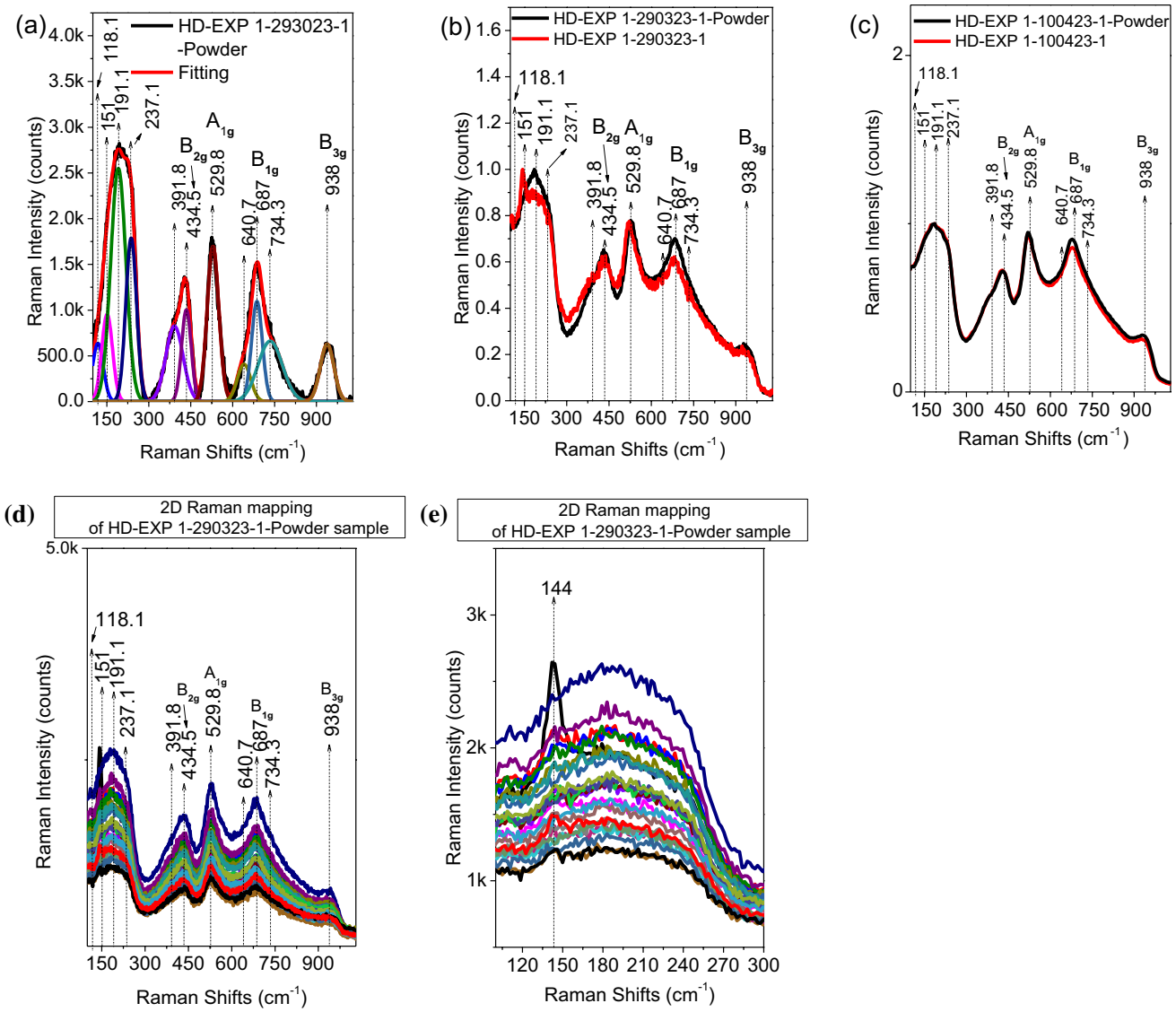


**Fig. 1** **a**–**c** Room temperature Raman spectra of the samples in Table 1. **d** 2D mapping Raman spectra of sample number 3 in Table 1. **e** Figure (**d**) plotted over 100–300 $cm^{-1}$. The positions of the Raman shifts reflect the results presented in Ref. [21]. No baseline added

On the one hand, Fig. 2 shows the crystallographic sites for Na atoms in the unit cell represented in the (a, e) a, (b, f) b, (c, g) c-direction and (d, h) in 3 dimensions. On the other hand, Fig. 3 shows a combination of crystallographic sites for the O and F atoms in the unit cell represented in the (a, e, i, m) a, (b, f, j, n) b, (c, g, k, o) c- direction and (d, h, l, p) in 3 dimensions. As in our previous work [21], we first associate the shortest bond-length vibration (Na(1)-F(4)) (see Figs. 2d and 3p) with the Raman shift observed at 938 $cm^{-1}$ in Fig. 1. This is the Raman shift $B_{3g}$. Secondly, the vibrational modes involving Na(1)-F(2–3) and Na(3)-F(2) bonds (see Fig. 2a–d, e–h and Figs. 3h, l) are attributed to the Raman shifts observed between 600 and 800 $cm^{-1}$. The peak at 687 $cm^{-1}$ is again provisionally attributed to the $B_{1g}$ atomic vibration mode. In addition, the peak at 529.8 $cm^{-1}$ is assumed to be associated with all Na–O vibrations: the $A_{1g}$ atomic vibration mode. The other peaks below 500 $cm^{-1}$ are probably associated with the remaining Na–F bonds. We have provisionally associated the shift at 434.5 $cm^{-1}$ with the $B_{2g}$ atomic vibration mode.

**Table 2** Room temperature Raman spectra of the sample HD-EXP 1-2h-290323-1-Powder number 3 in Table 1

| Peak | As prepared powder | | | | |
|---|---|---|---|---|---|
| | Type | Amplitude | Center | FWHM | Raman shift identification |
| 1 | Gauss + Lor | 636.8 | 118.1 | 45.3 | – |
| 2 | Gauss + Lor | 955.4 | 150.9 | 45.3 | – |
| 3 | Gauss + Lor | 2549.1 | 191.0 | 64.0 | – |
| 4 | Gauss + Lor | 1788.5 | 237.0 | 45.3 | – |
| 5 | Gauss + Lor | 825.3 | 391.8 | 72.6 | – |
| 6 | Gauss + Lor | 1003.3 | 434.4 | 40.4 | $B_{2g}$ |
| 7 | Gauss + Lor | 1696.6 | 529.7 | 48.8 | $A_{1g}$ |
| 8 | Gauss + Lor | 408.9 | 640.7 | 56.6 | |
| 9 | Gauss + Lor | 1095.1 | 687 | 45.3 | $B_{1g}$ |
| 10 | Gauss + Lor | 661.2 | 734.3 | 102.5 | |
| 11 | Gauss + Lor | 627.0 | 938.0 | 57.8 | $B_{3g}$ |

For further investigation of the powder phase, Fig. 4 shows an XRD analysis. XRD analysis was carried out only on sample number 3 (see Table 1), as it will be the subject of further experimental investigations, and the Raman spectra in Fig. 1 showed that all the samples developed have the same crystalline structure. Figure 4 shows the X-ray diffraction patterns obtained from the HD-EXP 1-2h-290323-1 powder. For better clarification, the intensities of the X-ray diffraction patterns are shown between (a–e) 10 and 35°, (b–f) 30 and 51°, (c–g) 50 and 70° and (d–h) 70 and 100°. On the one hand, the simulated diffraction of $Na_5(Ti_3O_3F_{11})$ powder (red lines) is added to the figures Fig. 4a–d as a reference, as this is the molecule that has been identified to match the electron diffraction patterns collected from plates developed on FTO, according to reference [21]. On the other hand, in order to investigate the origin of the Raman peak observed at 144 $cm^{-1}$ (see Fig. 1e), a simulated powder diffraction pattern of anatase $TiO_2$ (blue lines) (using Visualization for Electronic and Structural Analysis (VESTA 3.5.8) [26]) is added to Fig. 4e–h as a reference. In fact, $TiO_2$ in the anatase phase is known to cause a Raman shift at 144 $cm^{-1}$.

Figure 4a–d show that some X-ray diffracting crystal planes are not considered in the calculated diffraction patterns of $Na_5(Ti_3O_3F_{11})$, such as the planes diffracting at $2\theta = 13.78°$, $2\theta = 27.3°$, $2\theta = 32.56°$, $2\theta = 33.22°$, $2\theta = 36.34°$, $2\theta = 37.58°$, $2\theta = 38.7°$, $2\theta = 53.74°$,

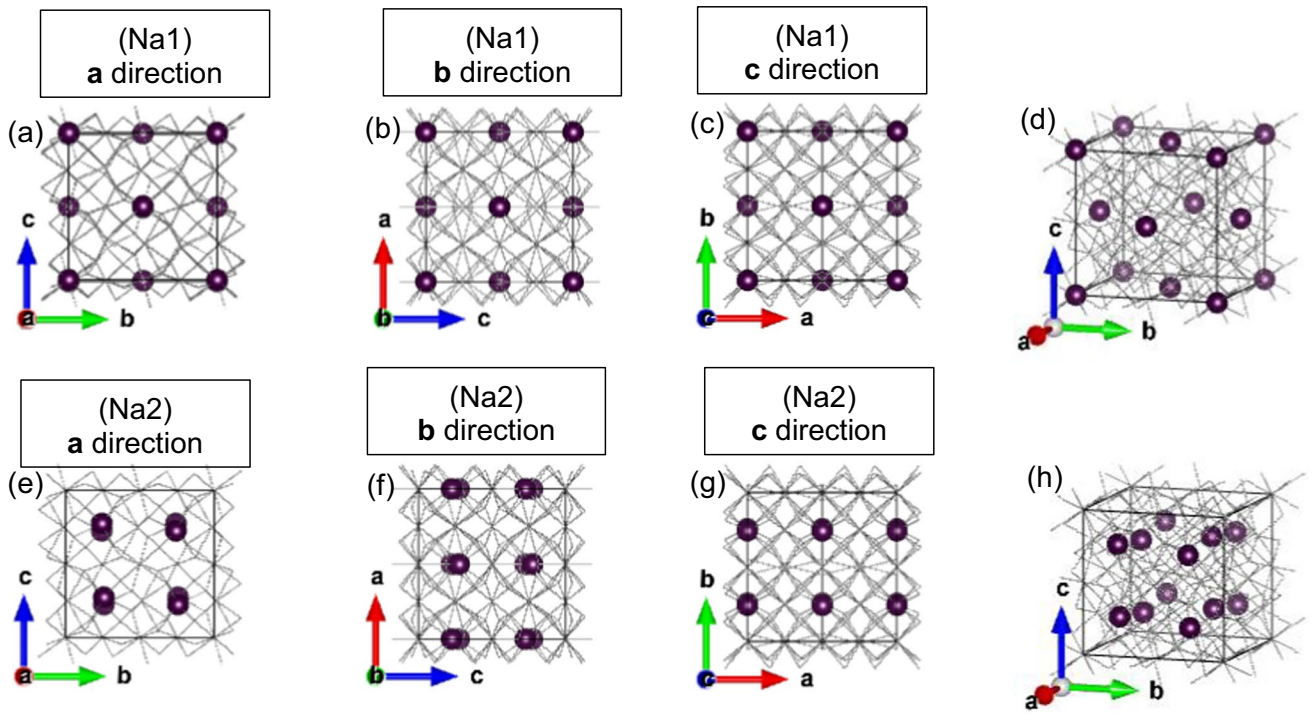


**Fig. 2** Crystallographic sites for atoms of Na in the unit cell shown in the **a**, **e** a direction, **b**, **f** b direction, **c**, **g** c-direction and **d**, **h** in 3 dimensions. Specific names of sites are indicated in the figures. Black ball = Na

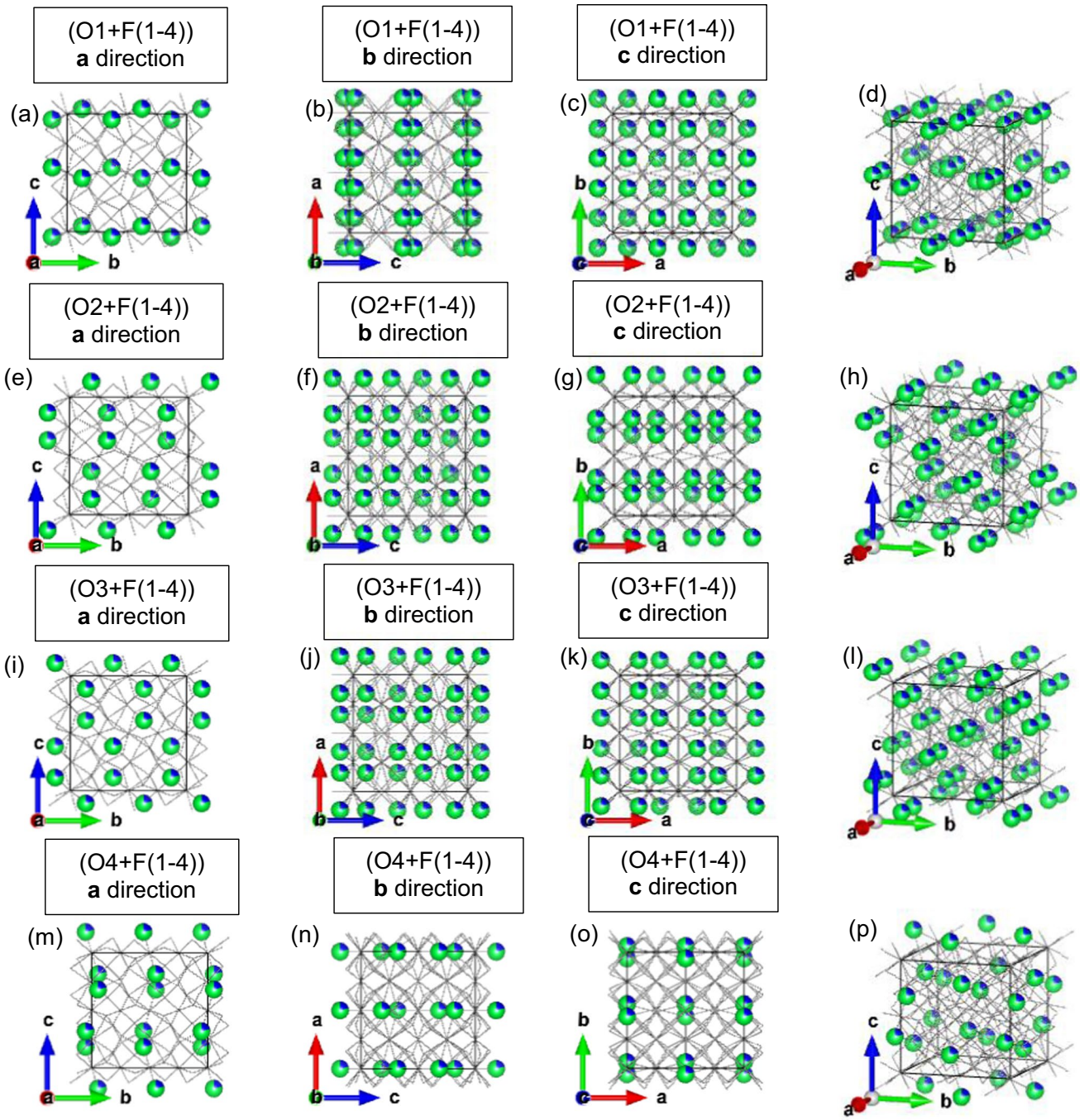


**Fig. 3** Crystallographic sites for atoms of O and F in the unit cell shown in the **a**, **e**, **i**, **m** a direction, **b**, **f**, **j**, **n** b direction, **c**, **g**, **k**, **o** c-direction and **d**, **h**, **l**, **p** in 3 dimensions. Specific names of sites are indicated in the figures. Blue balls = O, and green balls = F

2θ = 56.38°, 2θ = 57.58°, 2θ = 61.42°, 2θ = 63.68°, 2θ = 66.9°, 2θ = 69.2°, 2θ = 72.42°, 2θ = 82.9°, 2θ = 84.64°, 2θ = 84.96°, 2θ = 89.6°, 2θ = 90.38°, 2θ = 97.54°, 2θ = 97.8°, to name a few. Figure 4e–h show that X-ray diffracting crystal planes not considered as pointed out in Fig. 4a–d, are still not considered in the calculated diffraction patterns of anatase-phase $TiO_2$. The structures thus developed by the hydrothermal method may be of a different phase than that reported by Grannec et al. [27], and of a different stoichiometry than that of $Na_5(Ti_3O_3F_{11})$ (different from what was published in reference [21]) or may be a mixture of two materials namely $Na_5(Ti_3O_3F_{11})$ and the compound responsible for the Raman shift observed at 144 $cm^{-1}$ (see Fig. 1e) that is not anatase-phase $TiO_2$. The Rietveld refinement analysis based on the XRD data presented in Fig. 4 is the topic of further work.

In fact, pentasodium trioxoundecafluoro-trititanate ($Na_5(Ti_3O_3F_{11})$) has been known since 1987 to exhibit three phase transitions at 120 ± 10 K, 260 ± 10 K and 770 ± 10 K, respectively [27]. Further studies were therefore conducted with the powder whose XRD diffractions were discussed earlier to verify whether it exhibits the same phase transition behavior at high temperature.

Figure 5 shows the Raman spectra collected during the annealing experiment of "HD-EXP 1-2h-290323-1 powder" in an argon flow from 23 to 325 °C. Figure 5a shows a Raman spectrum collected from a selected point in the sample that does not exhibit the Raman shift of 144 $cm^{-1}$. The point selected for data acquisition gave the same Raman feature as observed in Fig. 1, except for the shift at 144 $cm^{-1}$. This point was, therefore, a very good starting point to follow the phase transitions of the powder by Raman spectroscopy as a function of annealing temperatures.

The following general observations were made from Fig. 5:

1. Fig. 5a–f shows an intensity interplay between the three main Raman shifts ($B_{2g}$, $A_{1g}$, $B_{1g}$, and $B_{3g}$) located in the Raman shift range of 300–1000 $cm^{-1}$ during annealing from 23 to 200 °C. When the annealing temperature reaches 200 °C, these main Raman shifts show the same intensities, as shown in Fig. 5f. Longer annealing at 200 °C does not affect the observed Raman shifts much (compare the red spectrum with the black spectrum in Fig. 5f).
2. Fig. 5g–h shows a significant broadening of the main Raman shifts mentioned in observation (1) ($B_{2g}$, $A_{1g}$, $B_{1g}$, and $B_{3g}$) with increasing the annealing temperature from 200 to 250 °C. Longer annealing at 275 °C results in a gradual disappearance of the $B_{2g}$, $A_{1g}$, $B_{1g}$, and $B_{3g}$ Raman shifts (see Fig. 5h).
3. Fig. 5i–j shows that when the powder is annealed from 300 to 325 °C, all the initial Raman shifts attributed to the initial crystalline structure completely disappear, namely $B_{2g}$, $A_{1g}$, $B_{1g}$, and $B_{3g}$. We observe a new series of Raman shifts attributable to a possible newly developed phase of the powder. Explicitly, the blue arrows in Fig. 5j show the new Raman shifts over the Raman shift range from 100 to 2000 $cm^{-1}$.

In order to better understand observations (1–3), the Raman shifts presented in Fig. 1 were adjusted with what was reported in reference [21]. Specifically, the Raman peak positions reported in reference [21] were used to produce the fits shown in Figs. 6 and 11 to better track the effects of annealing. It should be noted that Figs. 6, 7, 8, 9, 10, 11 show Raman spectra at elevated temperatures.

Figure 6a–e shows the high-temperature fitted Raman spectra of the powder shown in Fig. 5 as a function of annealing in the 23–250 °C temperature range. The fitting of the Raman shifts follows the fitting procedures used in reference [21], such as the addition of a baseline and the nature of the fitting curves (Gauss + Lor). Table 3 provides more details on the changes identified in Fig. 6. Figure 6 shows the disappearance of the peak initially observed at 640.7 $cm^{-1}$ after annealing the powder at 100 °C. In addition, when annealed at 250 °C, the following peaks are extinguished: 370.4 $cm^{-1}$, $B_{1g}$ (a t 681.7 $cm^{-1}$) and 763.0 $cm^{-1}$. For a better understanding of Fig. 6, the positions of the Raman shift peaks as adjusted therein and the maximum width at half maximum (FWHM) as a function of annealing temperature in the temperature range from 23 to 250 °C are shown in Figs. 7 and 8, respectively. Peaks are numbered from 1 to 10, from left to right in the figures.

On one hand, Fig. 7 shows the positions of the Raman shifts as a function of annealing temperature in the temperature range of 23–250 °C. Due to possible fitting inconsistencies, an error of ± 0.2 $cm^{-1}$ has been added. The following observations were made: (i) first, a blue shift of peak 1 (follow the blue arrow in Fig. 7a) when annealing the powder in the temperature range of 51–150 °C, and second, a red shift of the same peak when annealing at 250 °C; (ii) peaks 2 and 3 are red-shifted when annealing the powder at 150 °C, and then blue-shifted when the temperature is 250 °C (see Fig. 7b, c); (iii) peaks 4 and 5 are blue-shifted only when the annealing temperature is set to 250 °C (see Fig. 7d, e); (iv) peak 6 ($B_{2g}$) is blue-shifted when the annealing

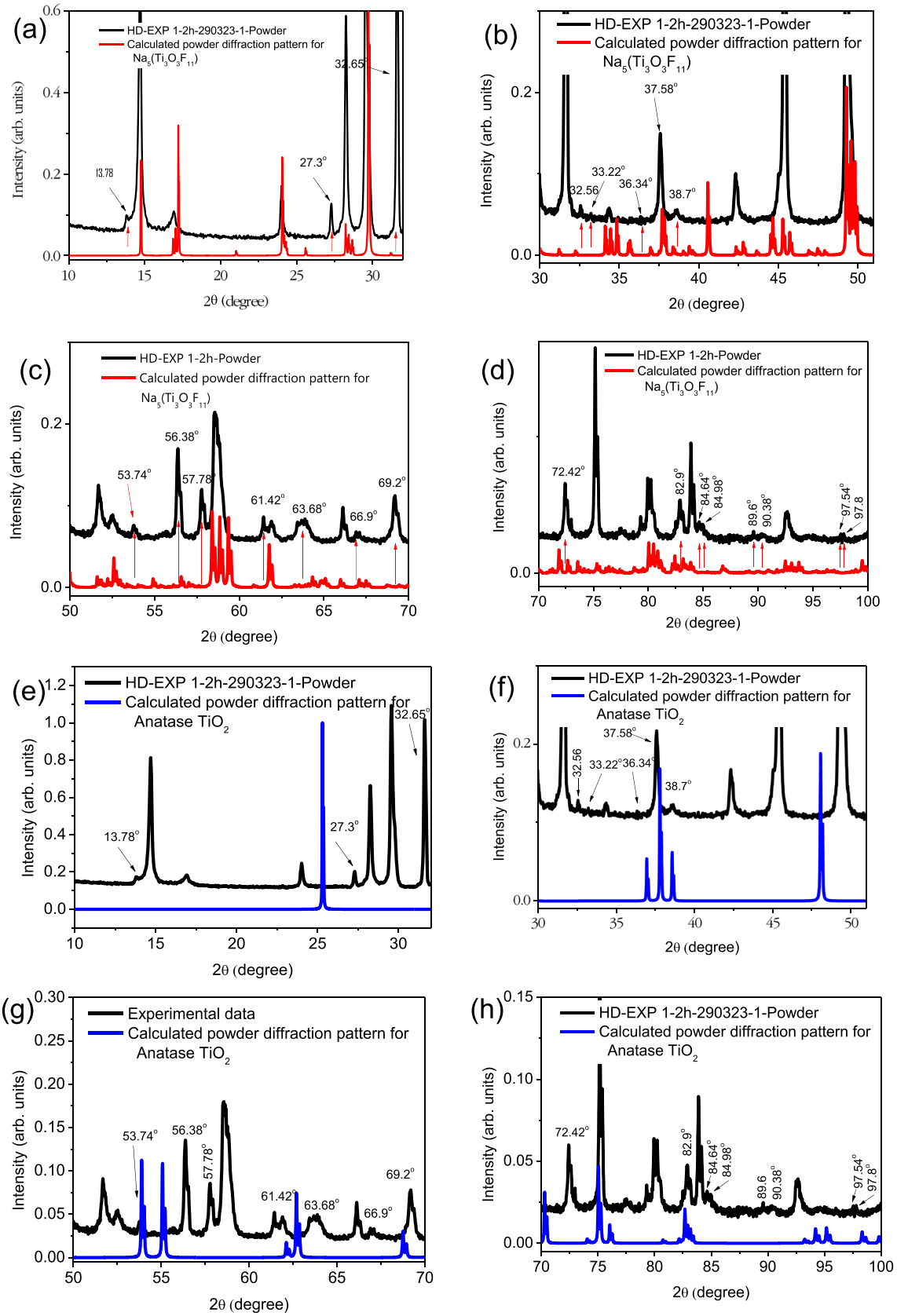
(a)
HD-EXP 1-2h-290323-1-Powder
Calculated powder diffraction pattern for Na5(Ti3O3F11)
13.78
27.3°
32.65°
Intensity (arb. units)
2θ (degree)
(b)
HD-EXP 1-2h-290323-1-Powder
Calculated powder diffraction pattern for Na5(Ti3O3F11)
37.58°
33.22°
32.56
36.34°
38.7°
Intensity (arb. units)
2θ (degree)
(c)
HD-EXP 1-2h-Powder
Calculated powder diffraction pattern for Na5(Ti3O3F11)
56.38°
53.74°
57.78°
61.42°
63.68°
66.9°
69.2°
Intensity (arb. units)
2θ (degree)
(d)
HD-EXP 1-2h-Powder
Calculated powder diffraction pattern for Na5(Ti3O3F11)
72.42°
82.9°
84.64°
84.98°
89.6°
90.38°
97.54°
97.8
Intensity (arb. units)
2θ (degree)
(e)
HD-EXP 1-2h-290323-1-Powder
Calculated powder diffraction pattern for Anatase TiO2
13.78°
27.3°
32.65°
Intensity (arb. units)
2θ (degree)
(f)
HD-EXP 1-2h-290323-1-Powder
Calculated powder diffraction pattern for Anatase TiO2
37.58°
32.56
33.22°
36.34°
38.7°
Intensity (arb. units)
2θ (degree)
(g)
Experimental data
Calculated powder diffraction pattern for Anatase TiO2
53.74°
56.38°
57.78°
61.42°
63.68°
66.9°
69.2°
Intensity (arb. units)
2θ (degree)
(h)
HD-EXP 1-2h-290323-1-Powder
Calculated powder diffraction pattern for Anatase TiO2
72.42°
82.9°
84.64°
84.98°
89.6
90.38°
97.54°
97.8°
Intensity (arb. units)
2θ (degree)

◂**Fig. 4** X-ray diffraction patterns obtained from HD-EXP 1-2h-290323-1 powder. For better clarification, the intensities of the X-ray diffraction patterns are shown between **a**–**e** 10 and 35°, **b**–**f** 30 and 51°, **c**–**g** 50 and 70° and **d**–**h** 70 and 100 °C. On the one hand, the simulated diffraction of $Na_5(Ti_3O_3F_{11})$ powder (red spectrum) is added to the figures (**a**–**d**) as a reference, as this is the compound that has been identified to match the electron diffraction patterns collected from plates developed on FTO, according to reference [21]. On the other hand, simulated powder diffraction of $TiO_2$ in anatase phase (blue spectrum) is added in figures (**e**–**h**) as reference, as $TiO_2$ in anatase phase is known to cause a Raman shift at 144 $cm^{-1}$

temperature is set to 250 °C; (v) peak 6 ($B_{2g}$) blue-shifts persistently under the defined annealing conditions (see Fig. 7f). Observations (i)–(v) show a general tendency for peaks 2 to 6 to shift towards the blue when the powder is annealed at over 150 °C. As we have seen above, we now understand that these Raman shifts are due to vibrational modes linked to the following bonds [21]: Na(2)-X (with X any of the fluorine anions located in crystallographic sites F1, F2, F3 and F4), Na(1)-F2, Na(3)-X (with X any of the fluorine anions located in sites F3 and F4). Consequently, annealing at 150 °C appears to strengthen/tighten the Na–F bonds highlighted above. Furthermore, (vi) peak 7 ($A_{1g}$) redshifts when the annealing temperature is set to 250 °C (see Fig. 7g); (vii) peak 8 ($B_{1g}$) and peak 9 begin to redshift when annealed at 51 °C (see Fig. 7h–i); and finally, (viii) peak 10 ($B_{3g}$) blue-shifts only when the annealing temperature is set at 250 °C as in (iii) (see Fig. 7j). From observations (vi) to (viii), it can be inferred that the peaks 7, 8 and 9 which are associated with vibrations involving Na(1)-X (with X representing F(2), F(3)), and Na(3)–F(2) bonds, respectively, persistently redshift with annealing up to at ~ 250 °C.

On the other hand, Fig. 8 shows FWHM (Full Width at Half Maximum) of the Raman shifts (discussed in Fig. 7) as a function of annealing temperature in the temperature range of 23–250 °C. In addition to the blue and red shifts observations discussed above (observations (i-vii)), the following can also be observed in Fig. 8: (ix) Fig. 8a shows a decrease in the width of peak 1 as a function of annealing temperature; (x) peak $A_{1g}$ (peak 7) broadens upon annealing at 250 °C (see Fig. 8b); (xi) peak $B_{1g}$ (peak 8) broaden upon annealing at 250 °C (see Fig. 8c); and finally, (xii) the FWHM of peak $B_{3g}$ (peak 10) decreases (see Fig. 8d).

For a better understanding, the temperature dependence of the positions and FWHMs for peak 1, peak 7 ($A_{1g}$), peak 8 ($B_{1g}$) and peak 10 ($B_{3g}$) are studied by approximation with the linear model and Klemens model equations presented in reference [28]. Indeed, the temperature dependence of all positions and the FWHM of experimentally observed Raman modes can be approximated by linear and Klemens models. According to the linear approximation model [28], the variation of Raman modes as function of annealing temperature T (°K)

$$\omega(T) = \omega_0 + \chi_{RM} T, \tag{2}$$

where $\omega_0$ is the optical phonon frequency at 0 K, $\chi_{RM}$ the temperature coefficient of shifts.

The variation of FWHM as function of T(°K) is given by

$$\Gamma(T) = \Gamma_0 + \chi_{FWHM} T, \tag{3}$$

where $\Gamma_0$ is the optical phonon frequency at 0 K, while $\chi_{FWHM}$ is the temperature coefficient associated with the FWHM of the modes.

According to the Klemens model [24, 28, 29],

$$\omega(T) = \omega_0 + \mathrm{A} \cdot \left(1 + \frac{2}{e^x - 1}\right) + \mathrm{B} \cdot \left[1 + \frac{3}{e^y - 1} + \frac{3}{(e^y - 1)^2}\right], \tag{4}$$

$$\Gamma(T) = \Gamma_0 + \mathrm{C} \cdot \left(1 + \frac{2}{e^x - 1}\right) + D \cdot \left[1 + \frac{3}{e^y - 1} + \frac{3}{(e^y - 1)^2}\right], \tag{5}$$

where, $\omega_0$ and $\Gamma_0$ are optical phonon energy and FWHM energy at 0 K, respectively; A, B, C and D are fitting parameters, and represents anharmonic constants related to three- and four-phonon processes, respectively; $x = \hbar\omega/2k_BT$ and $y = \hbar\omega/3k_BT$ with $k_B$ and $\hbar$ being the Boltzmann and Plank's constants. $\omega$ is the frequency of the laser light used by Raman spectroscopy. The fits of Eq. (2–5) to experimental data are shown in Figs. 9 and 10. It should be noted that Stanchik et al. [28] have used both models to quantitatively study the temperature dependence of Raman scattering in $Cu_2ZnSnSe_4$ thin films on a Ta foil substrate. Figures 9 and 10 show the linear approximations (blue line) and Klemens model (red curve) for the temperature dependence for the ten Raman shift positions discussed in Fig. 7, their FWHM temperature dependence. A summary of calculated values of A, B, C and D coefficients in Klemens model approximations for temperature dependence of shift positions and FWHM of all Raman modes are given in Table 4. Figures 9 and 10 show that the temperature dependence of the positions and FWHM for all observed Raman modes are non-linear. The Klemens model provides a much better approximation than the linear one. In addition, the Klemens model gives a perfect approximation of the temperature dependence of the FWHM for the same Raman modes. Consequently, since the approximation curves match the experimental data well,

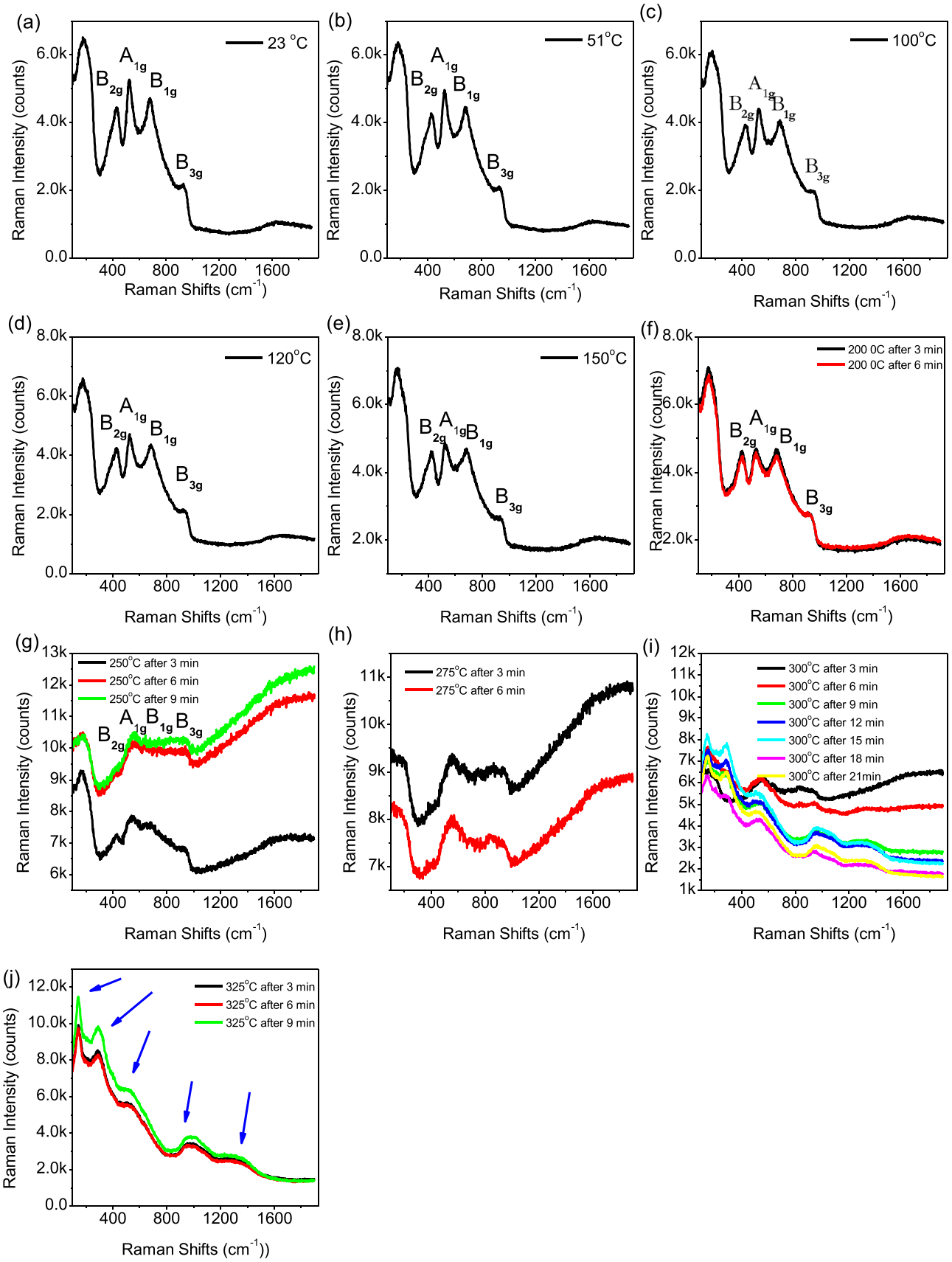
(a)
23 °C
(b)
51°C
(c)
100°C
(d)
120°C
(e)
150°C
(f)
200 0C after 3 min
200 0C after 6 min
(g)
250°C after 3 min
250°C after 6 min
250°C after 9 min
(h)
275°C after 3 min
275°C after 6 min
(i)
300°C after 3 min
300°C after 6 min
300°C after 9 min
300°C after 12 min
300°C after 15 min
300°C after 18 min
300°C after 21min
(j)
325°C after 3 min
325°C after 6 min
325°C after 9 min
A1g
B2g
B1g
B3g
Raman Intensity (counts)
Raman Shifts (cm-1)
Raman Shifts (cm-1))

◂**Fig. 5** Raman spectrum collected (**a**) at room temperature from a selected point on the sample that does not exhibit the 144 $cm^{-1}$ Raman shift; Raman spectrum collected at the same point as in (**a**) at **b** 51 °C, **c** 100 °C, **d** 120 °C, **e** 150 °C, **f** 200 °C, **g** 250 °C, **i** 275 °C, **j** 300 °C and **h** 325 °C, respectively. The blue arrows in figure (**j**) indicate the appearance of new Raman peaks during annealing at 325 °C

anharmonic phonon–phonon interactions are responsible for the observed temperature dependence of the Raman spectra of pentasodium trioxoundecafluoro-trititanate. Moreover, Table 4 shows that the values of anharmonic coefficients A and D for peaks 1, 2, 3, 4, 5, 6 (mode $B_{2g}$), 7 ($A_{1g}$) and 10 ($B_{3g}$) are greater than B and C, respectively. Similarly, the values of anharmonic coefficients A and D for peaks 8 and 9 ($B_{1g}$) are lower than B and C, respectively. We therefore understand that three- and four-phonon processes contribute to the damping process. Three- and four-phonon processes contribute to the observed shifts (peak 7 ($A_{1g}$), peak 8 ($B_{1g}$) and peak 9) ((observation i, vii and vii) and to the broadening of the FWHM (of peak 7 ($A_{1g}$) and peak 8 ($B_{1g}$)) (observations x and xi). These shifts are therefore attributed to the change in vibrational frequencies due to thermal expansion or the change in volume resulting from phonon softening induced by the increase in annealing temperature. However,

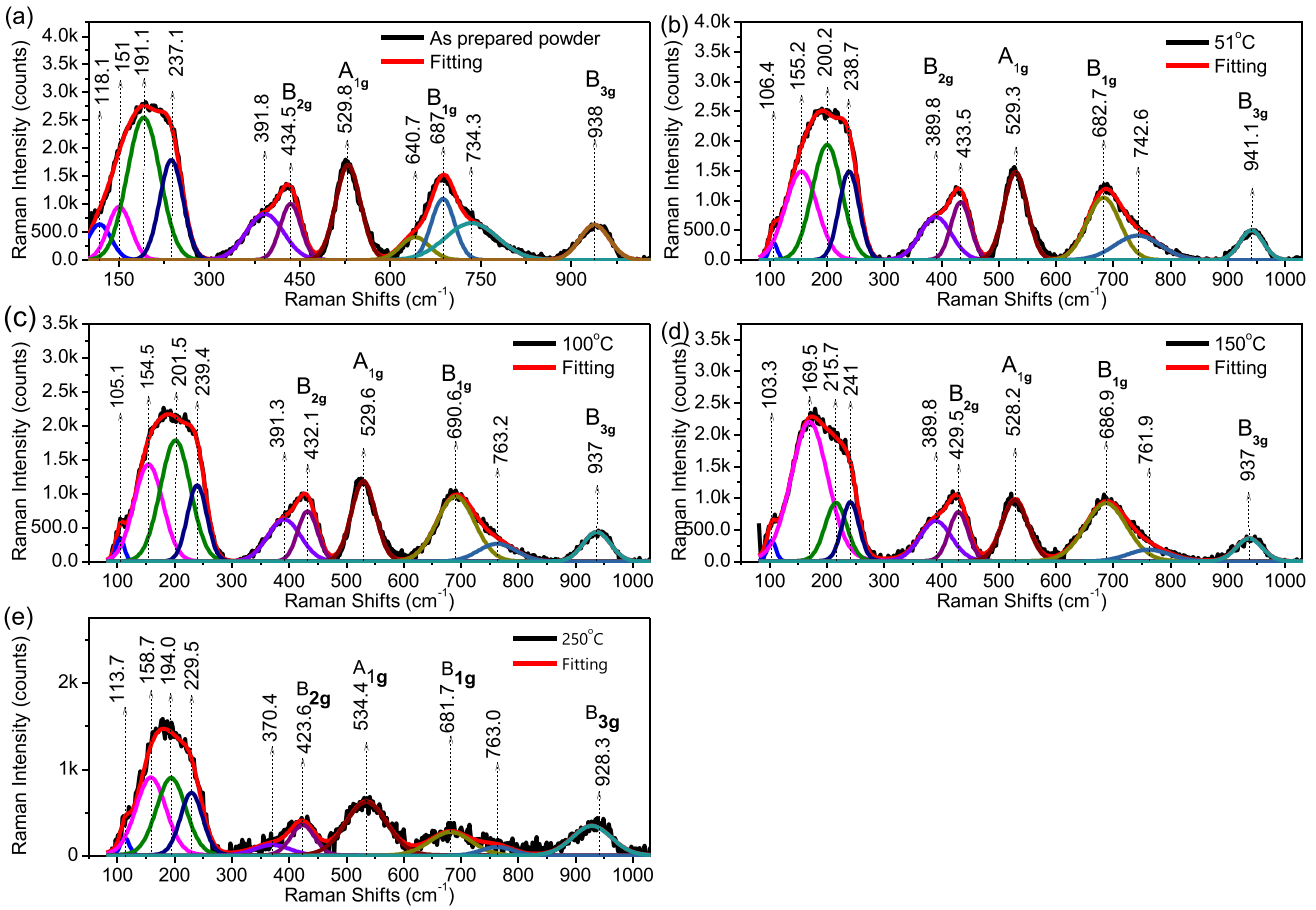


**Fig. 6** **a**–**e** Fitted high-temperature Raman spectra of the powder (HD-EXP 1-2h-290323-1-Powder) as a function of annealing in the temperature range 23–250 °C presented in Fig. 5. The fitting of the Raman shifts follows fitting procedures used in Ref. [21]

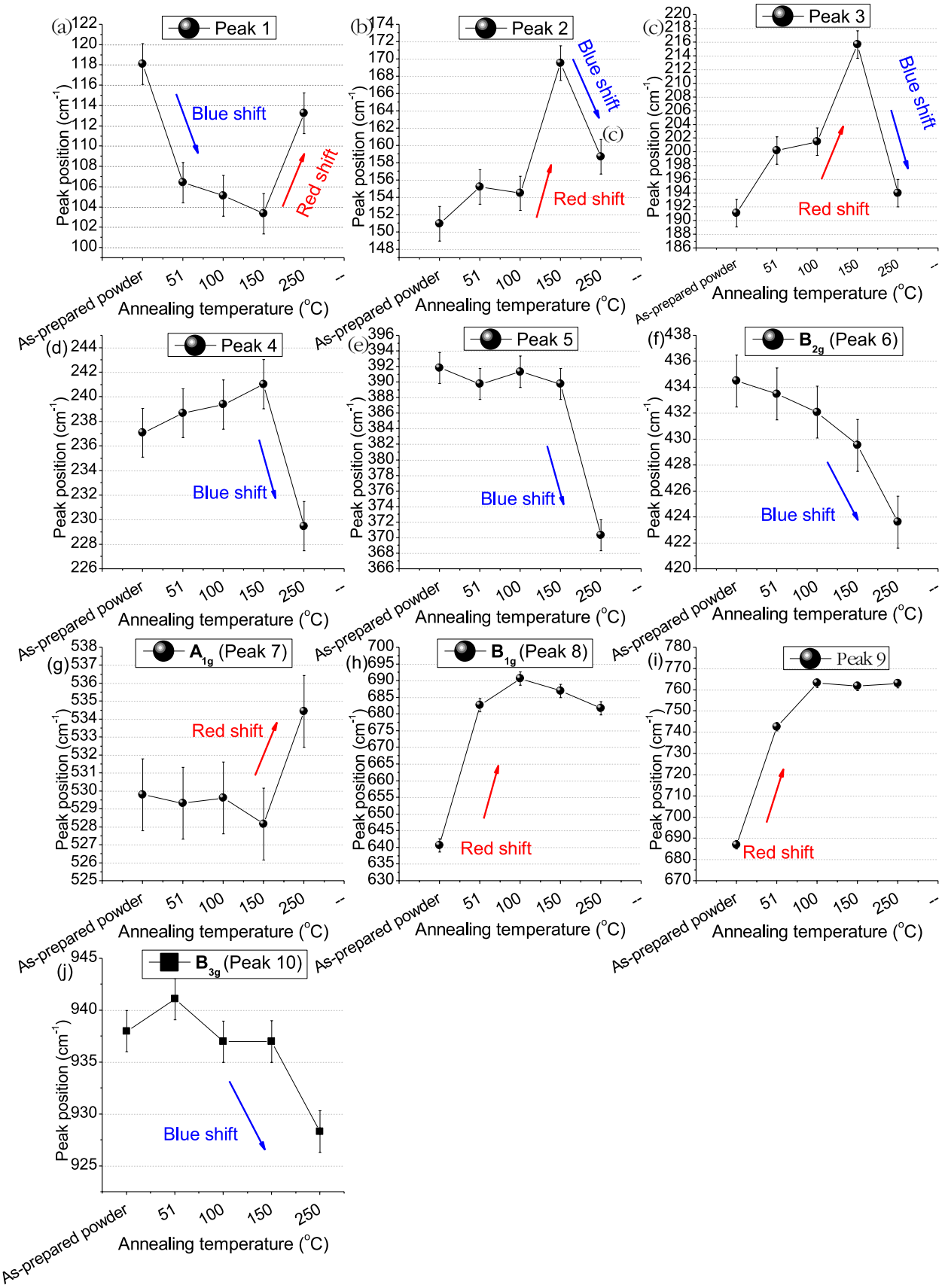
(a)
Peak 1
Blue shift
Red shift
Peak position (cm-1)
As-prepared powder
51
100
150
250
Annealing temperature (°C)
(b)
Peak 2
Blue shift
Red shift
(c)
Peak 3
Blue shift
Red shift
(d)
Peak 4
Blue shift
(e)
Peak 5
Blue shift
(f)
B2g (Peak 6)
Blue shift
(g)
A1g (Peak 7)
Red shift
(h)
B1g (Peak 8)
Red shift
(i)
Peak 9
Red shift
(j)
B3g (Peak 10)
Blue shift

◂**Fig. 7** Positions of Raman shifts as a function of annealing temperature over the 23–250 °C temperature range: **a** for peak 1, **b** peak 2, **c** peak 3, **d** peak 4, **e** peak 5, **f** $B_{2g}$ (peak6), **g** $A_{1g}$ (peak 7), **h** $B_{1g}$ (peak 8), **i** peak 9 and **j** $B_{3g}$ (peak 10). Due to possible fitting inconsistencies, an error of $\pm$ 2 $cm^{-1}$ has been added. Blue and red arrows are added to indicate blue and red Raman shift respectively

the observed blueshift (observations i, iii, iv–v and viii) are attributed to a modification in mean vibrational energy at constant volume. Explicitly, observations (i), (iii–v) and (viii) may have been caused by the compression of lattice parameters due to the phase transition that begins to occur during annealing at 250 °C.

Figure 11a shows the Raman spectra of the powder (HD-EXP 1-2h-290323-1-Powder) when the sample was further annealed at 250 °C, and (b) the addition of Raman shift fitting of the as prepared powder for comparison purposes. Figure 11b shows (xii) a redshift of the 527 $cm^{-1}$ peak as a function of annealing time (see the red arrow inserted in Fig. 11b). In addition, (xiii) all the Raman shifts observed in Fig. 6 are still present, but after longer annealing at 250 °C, they broaden. (xiv) There is also a peak that was not well

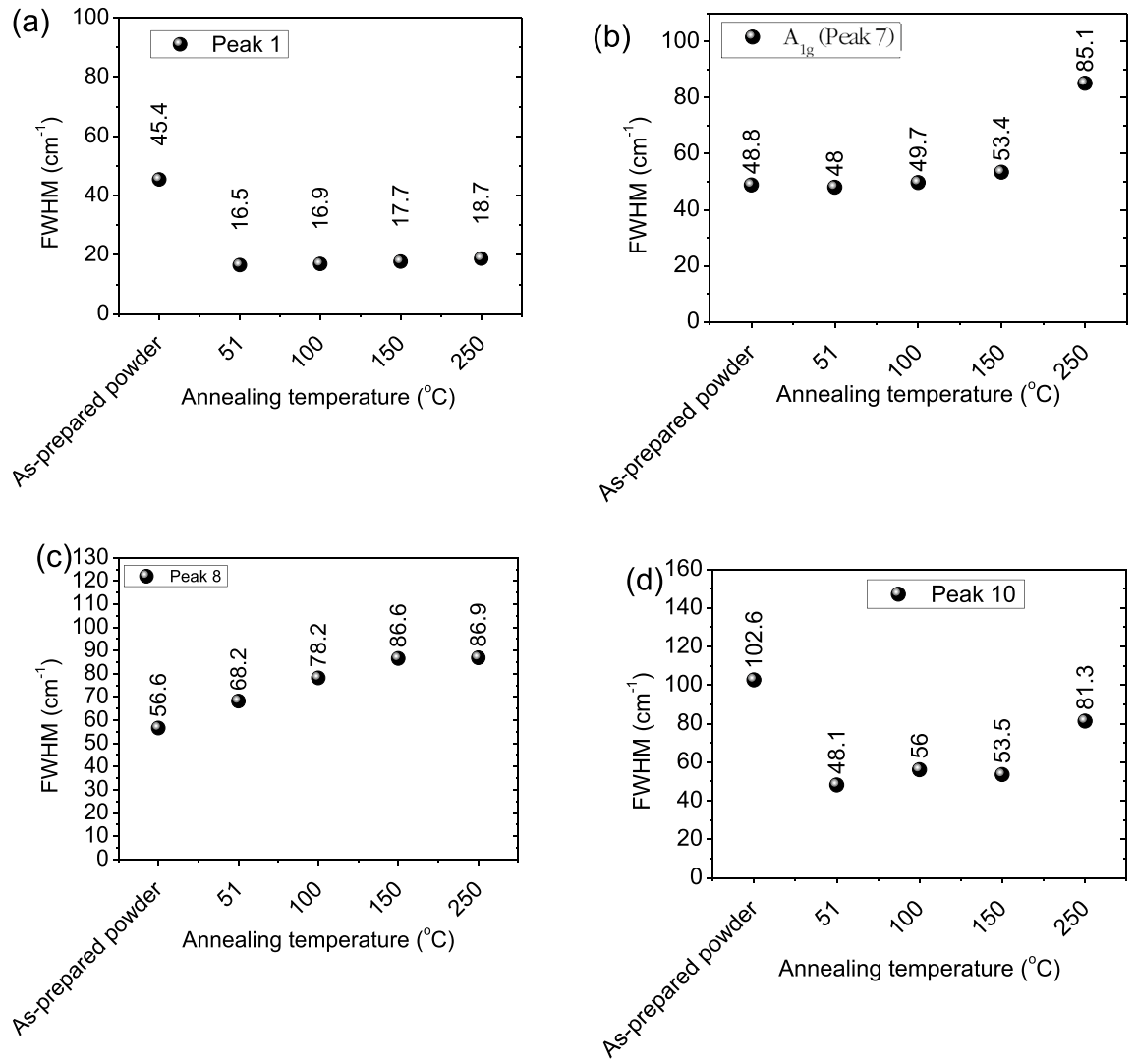


**Fig. 8** Full width at half maximum of Raman shifts as function of annealing temperature over the 23 to 250 °C temperature range: **a** for peak 1, **b** peak 2, **c** peak 3, **d** peak 4, **e** peak 5, **f** $B_{2g}$ (peak6), **g** $A_{1g}$ (peak 7), **h** $B_{1g}$ (peak 8), **i** peak 9 and **j** $B_{3g}$ (peak 10)

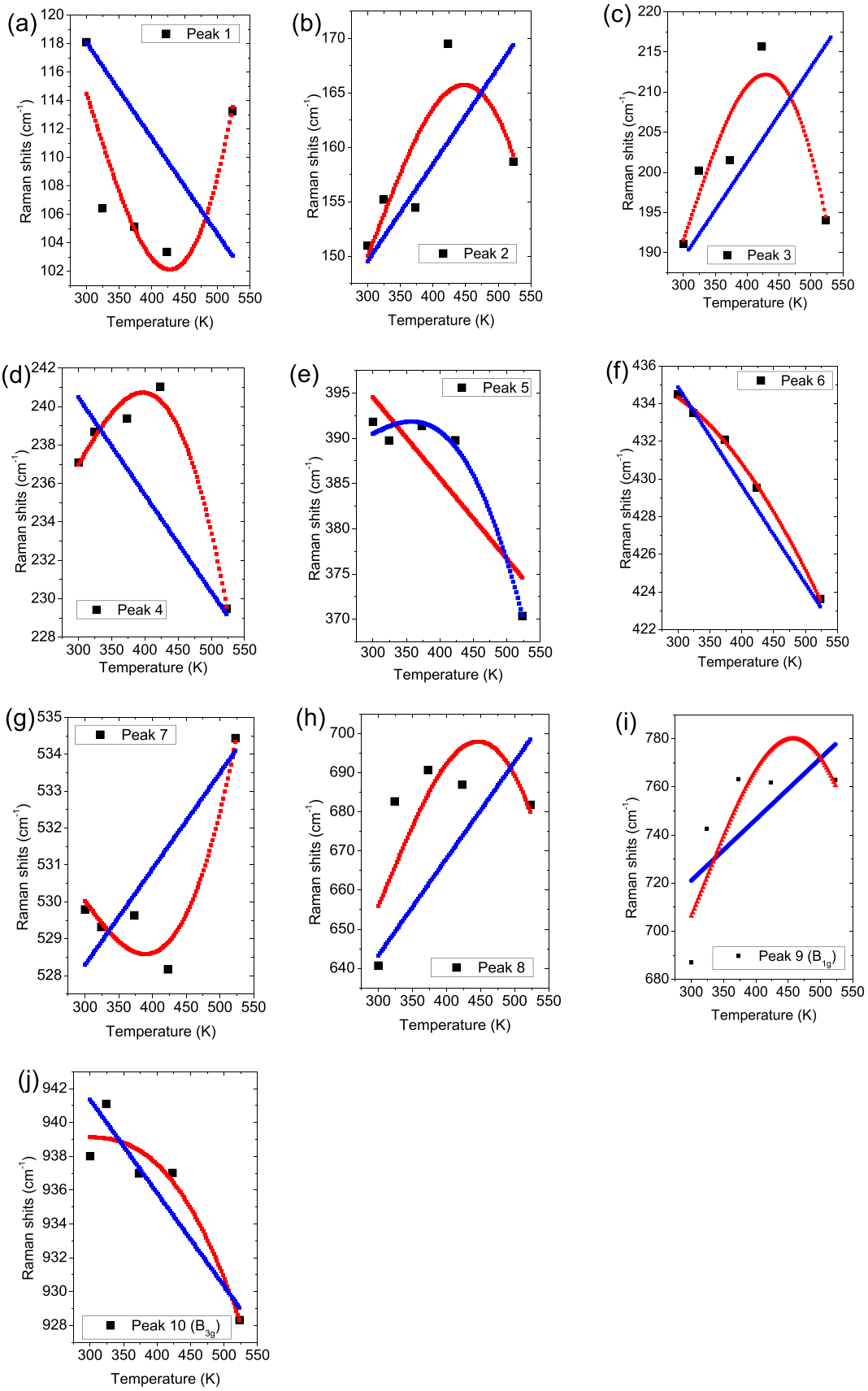
(a)
Peak 1
Raman shits (cm-1)
Temperature (K)
(b)
Peak 2
Raman shits (cm-1)
Temperature (K)
(c)
Peak 3
Raman shits (cm-1)
Temperature (K)
(d)
Peak 4
Raman shits (cm-1)
Temperature (K)
(e)
Peak 5
Raman shits (cm-1)
Temperature (K)
(f)
Peak 6
Raman shits (cm-1)
Temperature (K)
(g)
Peak 7
Raman shits (cm-1)
Temperature (K)
(h)
Peak 8
Raman shits (cm-1)
Temperature (K)
(i)
Peak 9 (B1g)
Raman shits (cm-1)
Temperature (K)
(j)
Peak 10 (B3g)
Raman shits (cm-1)
Temperature (K)

◂**Fig. 9** Linear approximations (blue line) and Klemens model (red curve) of temperature dependence for the ten Ramn shifts positions discussed in Fig. 7: **a** for peak 1, **b** peak 2, **c** peak 3, **d** peak 4, **e** peak 5, **f** $B_{2g}$ (peak6), **g** $A_{1g}$ (peak 7), **h** $B_{1g}$ (peak 8), **i** peak 9 and **j** $B_{3g}$ (peak 10)

resolved around 642.8 $cm^{-1}$ but is clearly visible in Fig. 11b (see inserted blue arrow). Longer annealing at 250 °C, as shown in Fig. 11, showed that pentasodium trioxoundecafluoro-trititanate begins to undergo a phase transition. For example, there is a peak which was not well resolved around 642.8 $cm^{-1}$ during the previous annealing, and which was enhanced by longer annealing at this temperature.

Figure 12 shows (a) Raman spectra of the same powder as a function of annealing in the temperature range 250–300 °C, and (b) the addition of Raman shift fitting of the as prepared powder for comparison purposes as in Fig. 11. Figure 12c and d shows the Raman spectra of the powder annealed at 300 °C in argon for ~ 21 min. The powder studied here was gradually annealed from 23 to 300 °C. Raman measurements were then made at this point as a function of annealing time at this temperature (300 °C). Recall that the position of the black-labelled peaks was determined in the powder at room temperature. Figure 12a, b shows (xv) the complete disappearance of the main peaks at 439 $cm^{-1}$ ($B_{2g}$) and 687 $cm^{-1}$ ($B_{1g}$). In addition, (xvi) the shift at 527 $cm^{-1}$ ($A_{1g}$) undergoes a further red shift as the annealing temperature increases. Figure 12c, d shows a complete phase transition. (xvii) The following Raman shifts have disappeared: $B_{2g}$ (439.5 $cm^{-1}$), $B_{1g}$ (686 $cm^{-1}$), 742.6 $cm^{-1}$. The new Raman shifts appeared as marked by red arrows in Fig. 12d. It is therefore understood that pentasodium trioxoundecafluoro-trititanate undergoes a complete phase transition when annealed at ~ 300 °C in argon.

To gain more understanding of these observations, the Raman spectrum obtained at 300 °C after a 15 min anneal presented in Fig. 12c, d was fitted and compared with the remaining Raman spectra obtained at 300 °C for different times. Figure 13 shows (a) fitted high-temperature Raman spectra of the powder (HD-EXP 1-2h-290323-1-Powder) annealed at 300 °C for 15 min. (xviii) The following new Raman shifts are observed: 147.0 $cm^{-1}$, 204.8 $cm^{-1}$, 285.5 $cm^{-1}$, 559.3 $cm^{-1}$, 943.1 $cm^{-1}$, 1045.3 $cm^{-1}$, 1237.2 $cm^{-1}$, 1341.7 $cm^{-1}$. A summary of these Raman shifts is given in Table 5. Figure 14 shows (a) Raman spectra of the powder (HD-EXP 1-2 h-290323–1-Powder) collected from the sample annealed at 325 °C (red spectrum), then cooled consecutively to 100 °C (green spectrum) and 30 °C (blue spectrum). Figure 14b shows fitting of the Raman spectrum cooled to 100 °C, (c) plot of Raman spectra in figures (a) and (b) on same axis, with the addition of baselines. The following (xix) new Raman shifts are identified: 149.7 $cm^{-1}$, 209.2 $cm^{-1}$, 303.6 $cm^{-1}$, 406.1 $cm^{-1}$, 529.2 $cm^{-1}$, 648.2 $cm^{-1}$, 929.5 $cm^{-1}$, 1000.5 $cm^{-1}$, 1076.9 $cm^{-1}$, 1149.6 $cm^{-1}$, 1229.1 $m^{-1}$, 1304.9 $cm^{-1}$and 1394.6 $cm^{-1}$. A summary of these Raman shifts is given in Table 6. Detailed calculations to establish the assignments of these peaks is the topic of further work.

## 4 Conclusion

We reported for the first-time experimental results of Raman spectroscopy as a function of temperature, measured from pentasodium trioxoundecafluoro-trititanate powder ($Na_5(Ti_3O_3F_{11})$) in a temperature range from room temperature to 325 °C. Two models were used to approximate the temperature-dependent Raman shift and the FWHM of the same Raman modes: linear and Klemens models. The Klemens model provided a much better approximation than the linear model. Consequently, anharmonic phonon–phonon interactions were considered to be responsible for the observed temperature dependence of the Raman spectra of pentasodium trioxoundecafluoro-trititanate. In addition, it was understood that three- and four-phonon processes contribute to the damping process. Observed redshifts and blueshifts were therefore attributed to the change in vibrational frequencies due to thermal expansion or to the change in volume resulting from phonon

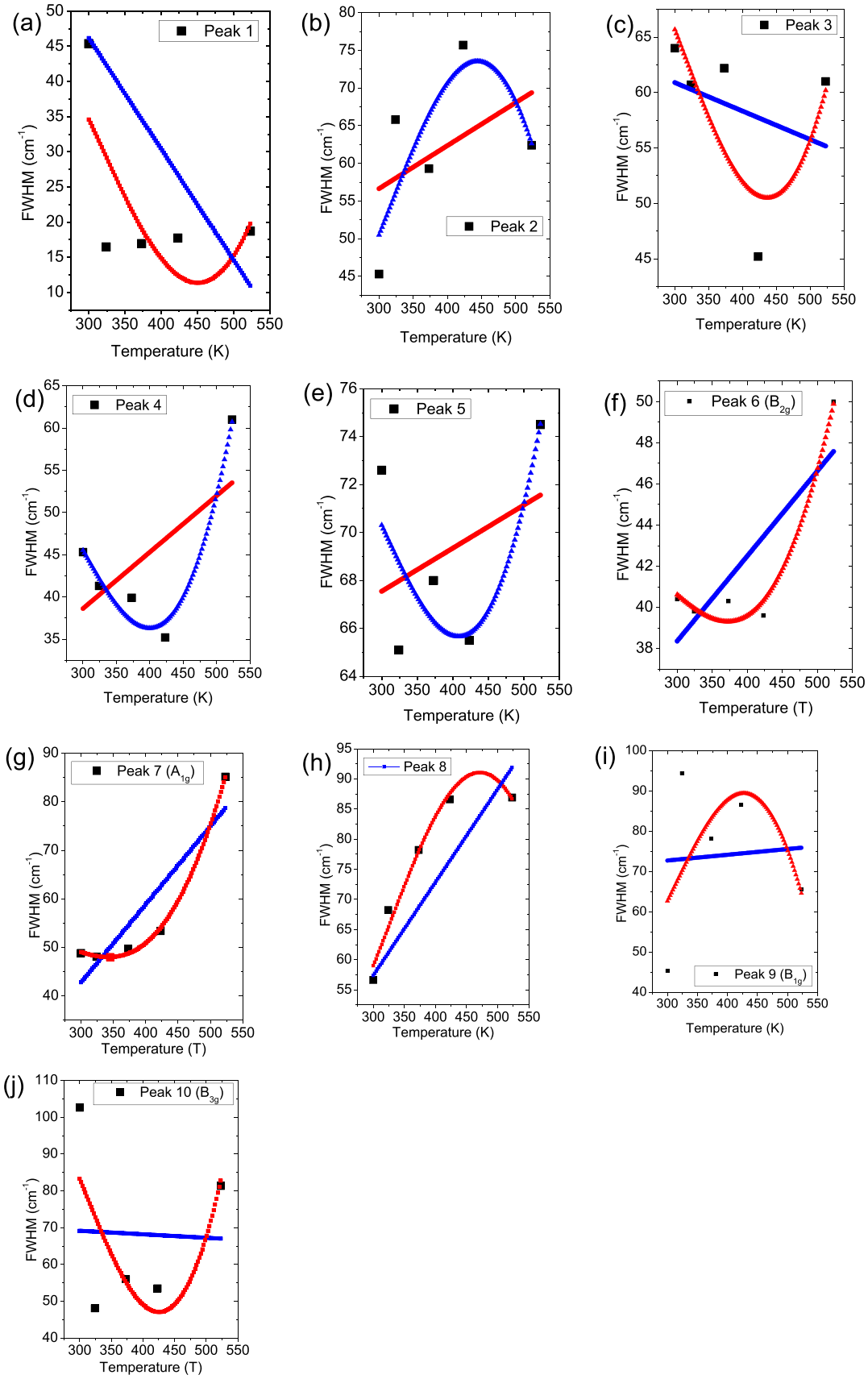
(a)
Peak 1
FWHM (cm-1)
Temperature (K)
(b)
Peak 2
FWHM (cm-1)
Temperature (K)
(c)
Peak 3
FWHM (cm-1)
Temperature (K)
(d)
Peak 4
FWHM (cm-1)
Temperature (K)
(e)
Peak 5
FWHM (cm-1)
Temperature (K)
(f)
Peak 6 (B2g)
FWHM (cm-1)
Temperature (T)
(g)
Peak 7 (A1g)
FWHM (cm-1)
Temperature (T)
(h)
Peak 8
FWHM (cm-1)
Temperature (K)
(i)
Peak 9 (B1g)
FWHM (cm-1)
Temperature (K)
(j)
Peak 10 (B3g)
FWHM (cm-1)
Temperature (T)

◂**Fig. 10** Linear approximations (blue line) and Klemens model (red curve) of temperature dependence for the FWHM of all peaks: **a** for peak 1, **b** peak 2, **c** peak 3, **d** peak 4, **e** peak 5, **f** $B_{2g}$ (peak6), **g** $A_{1g}$ (peak 7), **h** $B_{1g}$ (peak 8), **i** peak 9 and **j** $B_{3g}$ (peak 10)

softening induced by the increase in annealing temperature. However, the observed blue shifts were attributed to a change in mean vibrational energy at constant volume. In addition, $Na_5(Ti_3O_3F_{11})$ was found to undergo a phase transition at ~ 300 °C.

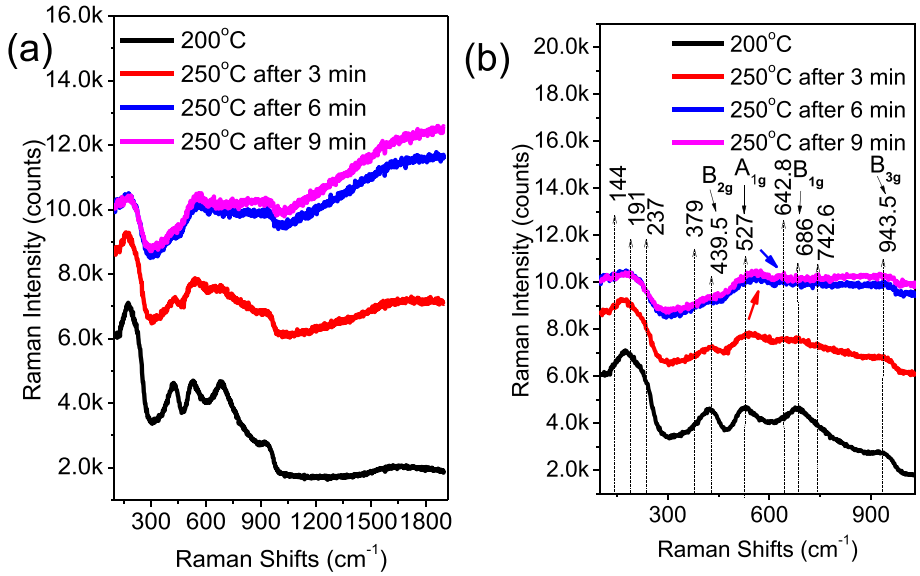


**Fig. 11** **a** High-temperature Raman spectra of the powder (HD-EXP 1-2h-290323-1-Powder) as a function of annealing in the temperature range 200–250 °C and **b** fitting of the corresponding Raman shifts. The fitting of the Raman shifts follows the results presented in Ref. [21]. No baseline added

**Table 3** Room and high temperature Raman spectra of the sample HD-EXP 1-2h-290323-1-Powder number 3 in Table 1 as function of annealing temperature

| Peak | As prepared powder | | | | | Raman shift identification |
|---|---|---|---|---|---|---|
| | Type | Amplitude | Center | FWHM | Comment | |
| 1 | Gauss + Lor | 636.8 | 118.1 | 45.3 | – | – |
| 2 | Gauss + Lor | 955.4 | 151 | 45.3 | – | – |
| 3 | Gauss + Lor | 2549.1 | 191.1 | 64.0 | – | – |
| 4 | Gauss + Lor | 1788.5 | 237.1 | 45.3 | – | – |
| 5 | Gauss + Lor | 825.3 | 391.8 | 72.6 | – | – |
| 6 | Gauss + Lor | 1003.3 | 434.5 | 40.4 | – | $B_{2g}$ |
| 7 | Gauss + Lor | 1696.6 | 529.8 | 48.8 | – | $A_{1g}$ |
| 8 | Gauss + Lor | 408.9 | 640.7 | 56.6 | – | – |
| 9 | Gauss + Lor | 1095.1 | 687 | 45.3 | – | $B_{1g}$ |
| 10 | Gauss + Lor | 661.2 | 734.3 | 102.5 | – | – |
| 11 | Gauss + Lor | 627.0 | 938 | 57.8 | – | $B_{3g}$ |

**Table 3** (continued)

| Peak | As prepared powder | | | | | Raman shift identification |
|---|---|---|---|---|---|---|
| | Type | Amplitude | Center | FWHM | Comment | |
| 51 °C | | | | | | |
| Peak | Type | Amplitude | Center | FWHM | Comment | Raman shift identification |
| 1 | Gauss + Lor | 291.6 | 106.4 | 16.4 | – | – |
| 2 | Gauss + Lor | 1492.7 | 155.2 | 65.8 | – | – |
| 3 | Gauss + Lor | 1938.6 | 200.2 | 60.7 | – | – |
| 4 | Gauss + Lor | 1488.9 | 238.7 | 41.3 | – | – |
| 5 | Gauss + Lor | 725.3 | 389.8 | 65.1 | – | – |
| 6 | Gauss + Lor | 974.8 | 433.5 | 39.8 | – | $B_{2g}$ |
| 7 | Gauss + Lor | 1479.4 | 529.3 | 48.0 | – | $A_{1g}$ |
| 8 | Gauss + Lor | 1050.9 | 682.7 | 68.2 | – | - |
| 9 | Gauss + Lor | 412.2 | 742.6 | 94.4 | – | $B_{1g}$ |
| 10 | Gauss + Lor | 498.3 | 941.1 | 48.0 | – | $B_{3g}$ |
| 100 °C | | | | | | |
| Peak | Type | Amplitude | Center | FWHM | Comment | Raman shift identification |
| 1 | Gauss + Lor | 343.6 | 105.1 | 16.9 | – | – |
| 2 | Gauss + Lor | 1430.2 | 154.5 | 59.3 | – | – |
| 3 | Gauss + Lor | 1784.6 | 201.5 | 62.2 | – | – |
| 4 | Gauss + Lor | 1124.2 | 239.4 | 39.9 | – | – |
| 5 | Gauss + Lor | 619.9 | 391.3 | 68.0 | – | – |
| 6 | Gauss + Lor | 741.7 | 432.1 | 40.3 | – | $B_{2g}$ |
| 7 | Gauss + Lor | 1182.1 | 529.6 | 49.6 | – | $A_{1g}$ |
| 8 | Gauss + Lor | 961.5 | 690.6 | 78.1 | – | |
| 9 | Gauss + Lor | 262.9 | 763.2 | 78.1 | – | $B_{1g}$ |
| 10 | Gauss + Lor | 434.8 | 937 | 55.9 | – | $B_{3g}$ |
| 150 °C | | | | | | |
| Peak | Type | Amplitude | Center | FWHM | Comment | Raman shift identification |
| 1 | Gauss + Lor | 333.1 | 103.3 | 17.7 | – | – |
| 2 | Gauss + Lor | 2202.9 | 169.5 | 75.7 | – | – |
| 3 | Gauss + Lor | 928.0 | 215.7 | 45.1 | – | – |
| 4 | Gauss + Lor | 939.3 | 241 | 35.2 | – | – |
| 5 | Gauss + Lor | 640.6 | 389.8 | 65.5 | – | – |
| 6 | Gauss + Lor | 783.0 | 429.5 | 39.6 | – | $B_{2g}$ |
| 7 | Gauss + Lor | 971.3 | 528.2 | 53.3 | – | $A_{1g}$ |
| 8 | Gauss + Lor | 922.5 | 686.9 | 86.5 | – | |
| 9 | Gauss + Lor | 187.0 | 761.9 | 86.5 | – | $B_{1g}$ |
| 10 | Gauss + Lor | 364.8 | 937 | 53.4 | – | $B_{3g}$ |
| 250 °C | | | | | | |

**Table 3** (continued)

| Peak | Type | Amplitude | Center | FWHM | Comment | Raman shift identification |
|---|---|---|---|---|---|---|
| 1 | Gauss + Lor | 207.7 | 113.7 | 18.6 | – | – |
| 2 | Gauss + Lor | 907.0 | 158.7 | 62.4 | – | – |
| 3 | Gauss + Lor | 900.8 | 194.0 | 61.0 | – | – |
| 4 | Gauss + Lor | 730.7 | 229.2 | 45.9 | – | – |
| 5 | Gauss + Lor | 125.9 | 370.4 | 74.5 | – | – |
| 6 | Gauss + Lor | 355.7 | 423.6 | 50.0 | – | $B_{2g}$ |
| 7 | Gauss + Lor | 621.4 | 534.4 | 85.1 | – | $A_{1g}$ |
| 8 | Gauss + Lor | 274.5 | 681.7 | 86.9 | – | - |
| 9 | Gauss + Lor | 101.9 | 762.0 | 67.5 | – | $B_{1g}$ |
| 10 | Gauss + Lor | 346.2 | 928.3 | 81.3 | – | $B_{3g}$ |

**Table 4** Calculated values of A, B, C and D coefficients in Klemens model approximations for temperature dependence of shift positions and FWHM of the Raman modes

| Peak (mode) | A ($cm^{-1}$) | B ($cm^{-1}$) | C ($cm^{-1}$) | D ($cm^{-1}$) | Observations | |
|---|---|---|---|---|---|---|
| | | | | | Raman shift | FWHM |
| Peak 1 | 5195.9 | − 816.0 | 6939.4 | − 1166.7 | $A \gg B$ | $C \gg D$ |
| Peak 2 | − 4870.0 | 812.3 | − 7520.9 | 1242.0 | $B \gg A$ | $C \ll D$ |
| Peak 3 | − 8397.7 | 1326.8 | 5507.4 | − 890.2 | $B \gg A$ | $C \gg D$ |
| Peak 4 | − 2793.0 | 393.8 | 6440.6 | − 918.6 | $B \gg A$ | $C \gg D$ |
| Peak 5 | − 3014.3 | 357.0 | 2730.6 | − 402.0 | $B \gg A$ | $C \gg D$ |
| Peak 6 ($B_{2g}$) | 122.4 | − 80.0 | 1810.8 | − 229.9 | $A \gg B$ | $C \gg D$ |
| Peak 7($A_{1g}$) | 1272.3 | − 174.1 | 4353.0 | 475.1 | $A \gg B$ | $C \gg D$ |
| Peak 8 | − 13,203.1 | 2195.9 | − 7395.6 | 1310.7 | $B \gg A$ | $C \ll D$ |
| Peak 9 ($B_{1g}$) | − 20,062.6 | 3437.4 | − 11,274.2 | 1769.9 | $B \gg A$ | $C \ll D$ |
| Peak 10 ($B_{3g}$) | − 823.1 | 67.3 | 15,643.4 | − 2443.2 | $B \gg A$ | $C \gg D$ |

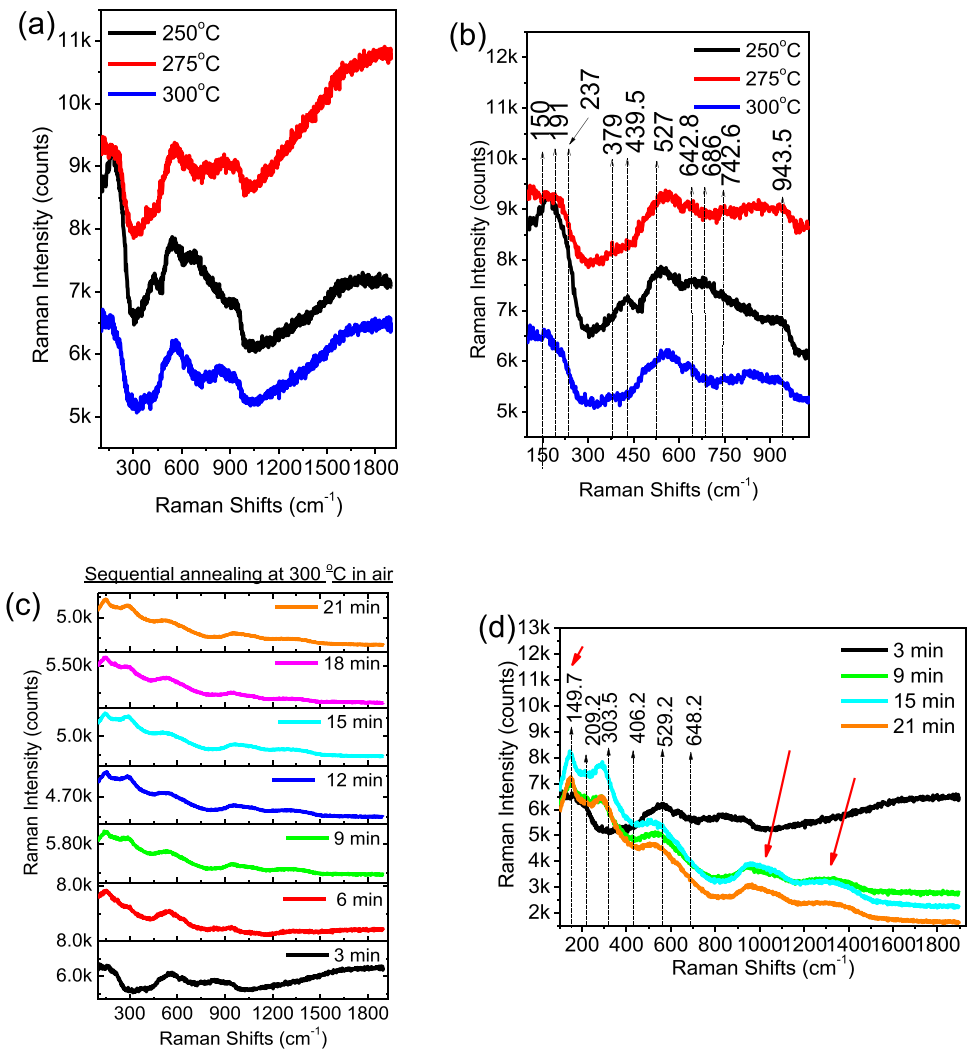


**Fig. 12** **a** High temperature Raman spectra of the powder (HD-EXP 1-2h-290323-1-Powder) as a function of annealing in the temperature range 250–300 °C and **b** fitting of the corresponding Raman shifts. The fitting of the Raman shifts follows the results presented in reference [21]. **c** Raman spectra of the powder annealed at 300 °C in argon for ~ 21 min and **d** fitting of the corresponding Raman shifts. No baseline added

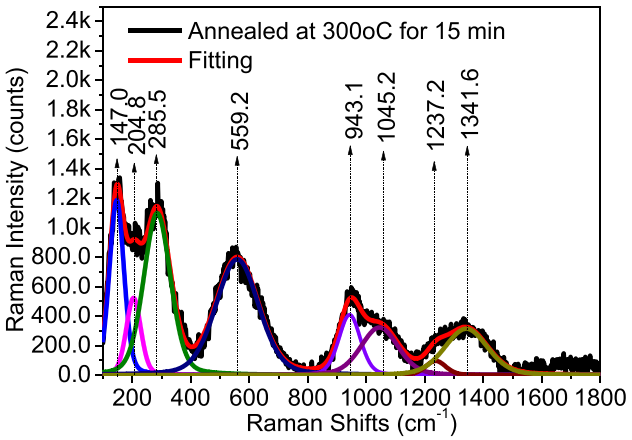


**Fig. 13** **a**, **b** Fitted high-temperature Raman spectra of the powder (HD-EXP 1-2h-290323-1-Powder) as a function of annealing times at 300 °C, presented in Fig. 12c–d

**Table 5** Summary of high temperature Raman shifts as observed from the powder (HD-EXP 1-2h-290323-1-Powder) annealed at 300 °C for 15 min

| Peak | Type | Amplitude | Center | FWHM | Comment | Raman shift identification |
|---|---|---|---|---|---|---|
| 1 | Gauss + Lor | 1185.8 | 147.0 | 59.3 | – | – |
| 2 | Gauss + Lor | 523.7 | 204.7 | 58.9 | – | – |
| 3 | Gauss + Lor | 1098.3 | 285.5 | 108.4 | – | – |
| 4 | Gauss + Lor | 785.9 | 559.2 | 173.1 | – | – |
| 5 | Gauss + Lor | 409.5 | 943.1 | 87.3 | – | – |
| 6 | Gauss + Lor | 323.1 | 1045.2 | 150.0 | – | – |
| 7 | Gauss + Lor | 97.3 | 1237.2 | 81.9 | – | – |
| 8 | Gauss + Lor | 314.8 | 1341.6 | 172.0 | – | – |

The fitted spectrum was taken from Fig. 12c

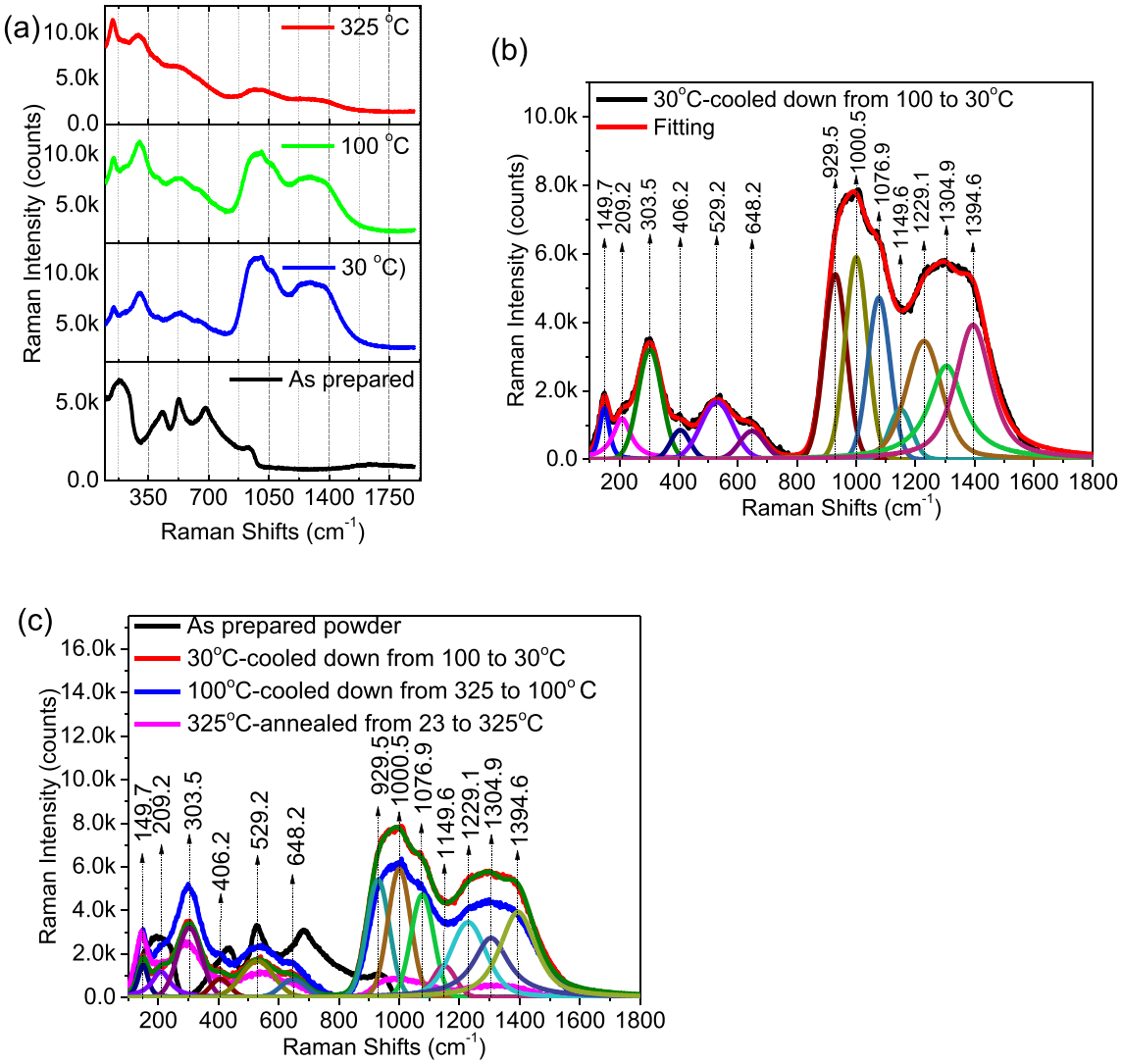


**Fig. 14** **a** Raman spectra of the powder (HD-EXP 1-2h-290323-1-Powder) collected from the sample annealed at 325 °C (red spectrum), then cooled consecutively to 100 °C (green spectrum) and 30 °C (blue spectrum). **b** Fitting of the Raman spectrum cooled to 100 °C. **c** Combination of figures **a** and **b** with baselines added to all spectra

**Table 6** Summary of room temperature (30 °C) Raman shifts as observed from the powder (HD-EXP 1-2h-290323-1-Powder) collected from the sample annealed at 325 °C, then cooled consecutively to 100 °C

| Peak | Type | Amplitude | Center | FWHM | Comment | Raman shift identification |
|---|---|---|---|---|---|---|
| 1 | Gauss + Lor | 1492.2 | 149.7 | 39.3 | – | – |
| 2 | Gauss + Lor | 1188.4 | 209.2 | 74.6 | – | – |
| 3 | Gauss + Lor | 3203.4 | 303.5 | 94.4 | – | – |
| 4 | Gauss + Lor | 854.2 | 406 | 76.0 | – | – |
| 5 | Gauss + Lor | 1670.5 | 529.2 | 127.3 | – | – |
| 6 | Gauss + Lor | 824.7 | 648.2 | 99.1 | – | – |
| 7 | Gauss + Lor | 5401.1 | 929.5 | 88.8 | – | – |
| 8 | Gauss + Lor | 5902.5 | 1000.4 | 88.8 | – | – |
| 9 | Gauss + Lor | 4722.0 | 1076.9 | 88.8 | – | – |
| 10 | Gauss + Lor | 1456.8 | 1149.5 | 88.8 | – | – |
| 11 | Gauss + Lor | 3454.8 | 1229.1 | 141.9 | – | – |
| 12 | Gauss + Lor | 2732.0 | 1304.9 | 141.9 | – | – |
| 13 | Gauss + Lor | 3925.6 | 1394.5 | 141.9 | – | – |

The fitted spectrum was taken from Fig. 14a

**Author contributions** All authors contributed to the design and development of the study. The material was prepared by C. M. Mbulanga, C. C. Ahia, K. S. Niyomugavyi and D. Harerimana. Data collection was carried out by C. M. Mbulanga, R. Erasmus and C. C. Ahia. Data analysis was carried out by C. M. Mbulanga, R. Erasmus, C. C. Ahia, K. S. Niyomugavyi, D. Harerimana and J. R. Botha. The first version of the manuscript was drafted by C. M Mbulanga, and all authors commented on earlier versions of the manuscript. All authors read and approved the final manuscript.

**Funding** This work was supported by the African Laser Center (Grant Number: ALC-R003).

**Data availability** Raw data were generated at the University of the Witwatersrand (School of Physics and Microscopy and Microanalysis Unit, WITS, Private Bag 3, Johannesburg, 2050, South Africa), the University of Fort Hare (Institute of Technology, Private Bag X1314, Alice, 5700, South Africa) and Nelson Mandela University (Department of Physics, P.O. Box 77000, Port Elizabeth, 6031, South Africa). Derived data supporting the results of this study are available on request from the corresponding author [CMM].

## Declarations

**Conflict of interest** The authors have no relevant financial or non-financial interests to disclose.

## References

1. R.R. Solís, J. Bedia, J.J. Rodríguez, C. Belver, Chem. Eng. J. **409**, 128110 (2021)
2. F. Suanon, Q. Sun, B. Dimon, D. Mama, C. Yu, J. Environ. Manag. **166**, 341 (2016)
3. S.M. Rodrigues, N. Cruz, C. Coelho, B. Henriques, L. Carvalho, A.C. Duarte, E. Pereira, P.F.A.M. Römkens, Environ. Pollut. **183**, 234 (2013)
4. T.W. Cheng, M.L. Lee, M.S. Ko, T.H. Ueng, S.F. Yang, Appl. Clay Sci. **56**, 90 (2012)
5. V.K. Gupta, I. Ali, T.A. Saleh, A. Nayak, S. Agarwal, RSC Adv. **2**, 6380 (2012)
6. M. Prica, S. Adamovic, B. Dalmacija, L. Rajic, J. Trickovic, S. Rapajic, M. Becelic-Tomin, Process. Saf. Environ. Prot. **94**, 262 (2015)
7. K. Lutchmiah, A.R.D. Verliefde, K. Roest, L.C. Rietveld, E.R. Cornelissen, Water Res. **58**, 179 (2014)
8. S. Alzahrani, A.W. Mohammad, J. Water Process Eng. **4**, 107 (2014)
9. U.T. Un, S.E. Ocal, Int. J. Environ. Sci. Dev. **6**, 425 (2015)
10. O.B. Akpor, M. Muchie, Int. J. Phys. Sci. **5**, 1807 (2010)
11. M. Zhao, S. Wang, H. Wang, Qin, D. Yang, Y. Sun, F. Kong, Environ. Pollut. **248**, 938 (2019)
12. P.Z. Ray, H.J. Shipley, RSC Adv. **5**, 29885 (2015)
13. L. di Bitonto, A. Volpe, M. Pagano, G. Bagnuolo, G. Mascolo, V. La Parola, D. Leo, C. Pastore, J. Hazard. Mater. **324**, 168 (2017)
14. D. Sounthararajah, P. Loganathan, J. Kandasamy, S. Vigneswaran, Chemosphere **168**, 467 (2017)
15. Y. Ishikawa, S. Tsukimoto, K.S. Nakayama, N. Asao, Nanoletter **15**(5), 2980 (2015)
16. J. Huang, Y. Cao, Z. Liu, Z. Deng, F. Tang, W. Wang, Chem. Eng. J. **180**, 75 (2012)
17. D. Yang, Z. Zheng, H. Liu, H. Zhu, X. Ke, Y. Xu, D. Wu, Y. Sun, J. Phys. Chem. C **112**, 16275 (2008)
18. Y. Hang, H. Yin, A. Wang, L. Shen, Y. Feng, R. Liu, Water Air Soil Pollut. **225**, 2095 (2014)
19. W. Liu, T. Wang, A.G.L. Borthwick, Y. Wang, X. Yin, X. Li, J. Ni, Sci. Total. Environ. **456–457**, 171 (2013)
20. H. Zhang, X.P. Gao, G.R. Li, T.Y. Yan, H.Y. Zhu, Electrochim. Acta **53**, 7061 (2008)
21. C.M. Mbulanga, R. Erasmus, J.E. Olivier, C.C. Ahia, E.L. Meyer, J.R. Botha, Open Ceramics **8**, 100181 (2021)
22. P.K. Sarswat, M.L. Free, A. Tiwar, Phys. Status Solidi **248**(9), 2170–2174 (2011)
23. O. Singh, N. Muhunthan, V.N. Singh, K. Samanta, N. Dilawar, Mater. Chem. Phys. **146**(3), 452–455 (2014)
24. A. Taube, A. Łapińska, J. Judek, N. Wochtman, M. Zdrojek, J. Phys. D Appl. Phys. **49**, 315301 (2016)
25. E. Kroumova, M.I. Aroyo, J.M. Perez-Mato, A. Kirov, C. Capillas, S. Ivantchev, H. Wondratschek, Phase Trans. **76**, 155 (2003)
26. K. Momma, F. Izumi, J. Appl. Crystallogr. **44**, 1272–1276 (2011)
27. J. Grannec, A. Yacoubi, J. Ravez, P. Hagenmuller, Solid State Commun. **62**, 407 (1987)
28. A.V. Stanchika, M.S. Tivanov, I.I. Tyukhovc, R. Juskenas, O.V. Korolik, V.F. Gremenok, A.M. Saad, A. Naujokaitis, Sol. Energy **201**, 480 (2020)
29. V.L. Deringer, R. Stoffel, R. Dronskowski, Phys. Rev. B **89**, 094303 (2014)